

THE ISAAC NEWTON TELESCOPE MONITORING SURVEY OF LOCAL GROUP DWARF GALAXIES. VI. THE STAR FORMATION HISTORY AND DUST PRODUCTION IN ANDROMEDA IX

HEDIEH ABDOLLAHI,¹ ATEFEH JAVADI,² MOHAMMAD TAGHI MIRTORABI,^{1,3} ELHAM SAREMI,^{2,4,5} JACCO TH. VAN LOON,⁶
HABIB G. KHOSROSHAHI,^{2,7} IAIN McDONALD,^{8,9} ELAHE KHALOUEI,² HAMIDREZA MAHANI,² SIMA TAEFI AGHDAM,² MARYAM SABERI,^{10,11}
AND MARYAM TORKI²

¹*Physics Department, Faculty of Physics and Chemistry, Alzahra University, Vanak, 1993891176, Tehran, Iran*

²*School of Astronomy, Institute for Research in Fundamental Sciences (IPM), PO Box 19395 – 5531, Tehran, Iran*

³*ICRANet, Piazza della Repubblica 10, I-65122 Pescara, Italy*

⁴*Instituto de Astrofísica de Canarias, VA Lctea s/n, 38205 La Laguna, Tenerife, Spain*

⁵*Departamento de Astrofísica, Universidad de La Laguna, 38205 La Laguna, Tenerife, Spain*

⁶*Lennard-Jones Laboratories, Keele University, ST5 5BG, UK*

⁷*Iranian National Observatory, Institute for Research in Fundamental Sciences (IPM), Tehran, Iran*

⁸*Jodrell Bank Centre for Astrophysics, Alan Turing Building, University of Manchester, M13 9PL, UK*

⁹*Department of Physical Sciences, The Open University, Walton Hall, Milton Keynes, MK7 6AA, UK*

¹⁰*Roseland Centre for Solar Physics, University of Oslo, P.O. Box 1029 Blindern, NO-0315 Oslo, Norway*

¹¹*Institute of Theoretical Astrophysics, University of Oslo, P.O. Box 1029 Blindern, NO-0315 Oslo, Norway*

ABSTRACT

We present a photometric study of the resolved stellar populations in And IX, the closest satellite to the M31, a metal-poor and low-mass dwarf spheroidal galaxy. We estimate a distance modulus of $24.56^{+0.05}_{-0.15}$ mag based on the tip of the red giant branch (TRGB). By probing the variability of asymptotic giant branch stars (AGB), we study the star formation history of And IX. We identified 50 long period variables (LPVs) in And IX using the Isaac Newton Telescope (INT) in two filters, Sloan i' and Harris V . In this study, we selected LPVs within two half-light radii with amplitudes in the range of 0.2 – 2.20 mag. It is found that the peak of star formation reaches $\sim 8.2 \pm 3.1 \times 10^{-4} M_{\odot} \text{ yr}^{-1}$ at ≈ 6 Gyr ago. Our findings suggest an outside-in galaxy formation scenario for And IX with a quenching occurring $3.65^{+0.13}_{-1.52}$ Gyr ago with the SFR in the order of $2.0 \times 10^{-4} M_{\odot} \text{ yr}^{-1}$ at redshift < 0.5 . We calculate the total stellar mass by integrating the star formation rate (SFR) within two half-light radii $\sim 3.0 \times 10^5 M_{\odot}$. By employing the spectral energy distribution (SED) fitting for observed LPVs in And IX, we evaluate the mass-loss rate in the range of $10^{-7} \leq \dot{M} \leq 10^{-5} M_{\odot} \text{ yr}^{-1}$. Finally, we show that the total mass deposition to the interstellar medium (ISM) is $\sim 2.4 \times 10^{-4} M_{\odot} \text{ yr}^{-1}$ from the C- and O-rich type of dust-enshrouded LPVs. The ratio of the total mass returned to the ISM by LPVs to the total stellar mass is $\sim 8.0 \times 10^{-10} \text{ yr}^{-1}$, and so at this rate, it would take ~ 1 Gyr to reproduce this galaxy.

Keywords: galaxies: Local Group – galaxies: individual: And IX – galaxies: stellar content – stars: evolution – stars: AGB and LPV – stars: mass-loss

1. INTRODUCTION

Dwarf galaxies are the most abundant type of galaxies in the Universe. They contain valuable information about the early Universe and its evolution (Cignoni & Tosi 2010). Dwarf galaxies also continue to play an important role in our understanding of galaxy formation and stellar evolution (Tolstoy 2003). Dwarf galaxies are divided into two main categories based on their gas content: gas-rich dwarfs: dwarf irregulars

(dIrrs), blue compact dwarfs (BCDs), and gas-poor dwarfs: dwarf ellipticals (dEs), dwarf spheroidals (dSphs), and ultra-faint dwarfs (UFDs) (Müller et al. 2021). The Local Group hosts various kinds of dwarf galaxies, and it is possible to study their resolved populations with space- or ground-based telescopes (Weisz et al. 2014).

Λ CDM, which is known as the standard model of cosmology, is compatible with most observations. In the Λ CDM, cold dark matter is assumed to be the dominant matter content of the Universe (Navarro 2018). In the hierarchical Λ CDM paradigm, galaxies evolve in dark matter halos formed in the early Universe by the gravitational collapse of overdense re-

gions. Moreover, the halos grow hierarchically through the accretion of subhalos. The galaxies are surrounded by these subhalos which are called satellite galaxies (Shi et al. 2020).

One of the main challenges for the cold dark matter scenario is the missing satellite problem (MSP) (Klypin et al. 1999; Del Popolo & Le Delliou 2017). There is a discrepancy between the number of satellites predicted in the CDM simulation and the observed satellites. There is also another critical challenge called Too Big To Fail. The N-body simulation, based on the Λ CDM, predicts that the satellites are too massive and dense compared to those observed (Boylan-Kolchin et al. 2011, 2012; Del Popolo & Le Delliou 2017). Thus, observing and studying dwarf galaxies enables us to understand the Universe and solve the aforementioned problems.

Several mechanisms (internal and external) could influence the evolution of dwarf galaxies. Compared to massive galaxies, dwarf galaxies have a smaller stellar population and a simple star formation history (SFH). There are internal processes, such as stellar feedback and depletion gas, and also environmental processes, such as tides and ram pressure stripping, that influence star formation in dwarf galaxies (Gnedin 2014; Wetzel et al. 2015; Xu et al. 2016; Simpson et al. 2018; Wheeler et al. 2019; Fillingham et al. 2019; Applebaum et al. 2021).

An optical monitoring survey was initiated using the Isaac Newton Telescope (INT) to study the SFH of dwarf galaxies in the Local Group by probing the asymptotic giant branch (AGB) stars (Saremi et al. 2020). Mass-loss is one of the notable features of AGB stars with large amplitude pulsations. These pulsations lead to long period photometric variability that can be observed in durable photometric campaigns (Javadi et al. 2011a). The INT survey was launched to estimate the dust ejected into the interstellar medium (ISM) and to determine the mass-loss rate in 55 nearby galaxies, spanning an order of magnitude in metallicity. The long period variables (LPVs) can be used to trace the stellar evolution and history of the galaxy. This survey allows us to compare the SFH in different galaxy types and to study the evolution and quenching times of dwarf galaxies. We used a method introduced by Javadi et al. (2011b, 2017) to build the SFH of the galaxy M33 and to estimate the dust ejection into the ISM.

AGBs and red supergiants (RSGs) are powerful tools to study SFH, as they have been presented in most of the history of the Universe (~ 10 Myr to 10 Gyr) and are in their final evolution stage, where their luminosity relates directly to their birth mass (Javadi et al. 2011b). Various surveys in the IR-wavelength have widely studied AGBs and RSGs (Javadi et al. 2011a, 2015; Battinelli & Demers 2013; Boyer et al. 2009, 2015a,b). Dust-producing LPVs are more easily detected in the optical bands because their amplitude is larger

compared to the IR-wavelength, though there has not yet been a comprehensive survey of long period variable stars in Local Group dwarf galaxies. In addition, the inclusion of IR bands in the spectral energy distributions (SED) makes the calculation of dust density more accurate, since optical color alone is not a sufficient indicator of dust density. The INT monitoring survey, thanks to a comprehensive sampling (to date), could address open questions about the evolution of dwarfs and shutting-down the star formation by various effects such as environmental processes and tidal effects.

AGB stars can reach a luminosity of $10^4 L_{\odot}$ (van Loon et al. 2005a) at their most luminous stage. These luminous populations are easily distinguished from the background, especially in the infrared, where the difference in brightness is very pronounced. These types of stars are cool with temperatures of $\lesssim 4000$ K (van Loon et al. 2005a), and have a birth mass of $0.8 M_{\odot} \leq M \leq 8 M_{\odot}$ (Höfner & Olofsson 2018). AGB stars consist of an electron-degenerate (C-O) core and two shells around it. Burning helium and hydrogen in the shells generates energy for evolution in AGBs. Helium shell burning releases considerable energy in a flash-like process, resulting in a long series of thermal pulses (Rosenfield et al. 2014). Periodic expansions and contractions of the outer layers lead to radial pulses, usually on the order of 10^2 to 10^3 days (Höfner & Olofsson 2018). Most stars (especially AGBs) experience mass-loss at the end of their evolution. Dust can be produced mainly in two environments: during the thermal pulsation phase in the cool and dense atmosphere of AGBs with low to intermediate stellar mass (0.8 - $8 M_{\odot}$), and during the core-collapse phase of stars with enough heavy mass ($M > 8 M_{\odot}$) to end their lives with supernova explosions (Valiante et al. 2009). AGB stars deposit some of their mass into the ISM through radial mechanical pulsation and thus play a crucial role in enriching the ISM. van Loon et al. (1999) estimated the mass-loss rate in the range of $10^{-7} < \dot{M} \leq 10^{-3} M_{\odot} \text{ yr}^{-1}$ based on a sample of AGBs and RSGs in the Large Magellanic Cloud (LMC).

In this paper, we focus on a spheroidal dwarf satellite along the major axis of M31 galaxy, And IX, which is closest to the host, and one of the least luminous satellites. And IX was discovered using the resolved stellar photometry of the Sloan Digital Sky Survey (SDSS) by Zucker et al. (2004) and categorized as an old dwarf galaxy with little baryonic matter. The term of old was due to the fact that no significant population of intermediate-age carbon and main sequence stars were observed with the WIYN 3.5-m telescope by Harbeck et al. (2005). Table 1 shows in detail the apparent characteristics of And IX, which was selected for this study for the following reasons:

- Studying one of the Andromeda satellites allows us to investigate whether the star-forming pattern and quenching time are consistent with those of the Milky

Table 1. Properties of And IX dwarf galaxy

RA.(J2000)	00 52 53	Zucker et al. (2004)
DEC.(J2000)	+43 11 45	Zucker et al. (2004)
M_V (mag)	-9.0 ± 0.3	Weisz et al. (2019a)
r_h (pc)	444^{+68}_{-53}	Weisz et al. (2019a)
[Fe/H] (dex)	-2.03 ± 0.01	Wojno et al. (2020)
σ (km s ⁻¹) ^a	$4.5^{+3.6}_{-3.4}$	Collins et al. (2010)
Σ_V (mag arcsec ⁻²) ^b	28.0 ± 1.2	McConnachie (2012)
V (mag) ^c	16.3 ± 1.1	Conn et al. (2012)

^aObserved velocity dispersion^bSurface brightness^cApparent magnitude in Vega magnitude system

Way. It also helps to understand whether this dwarf galaxy follows other M31 satellites in its formation scenario, as studied by Weisz et al. (2019b).

- And IX is an important case study because of its proximity to the host $\sim 39^{+5}_{-2}$ kpc (Weisz et al. 2019a), in which quenching time and galaxy evolution may have been affected by environmental effects such as the strong tidal effect of M31.
- With a mass-to-light ratio of $1 M_{\odot}/L_{\odot}$, McConnachie (2012) estimated the dynamical mass ($6.5 \times 10^6 M_{\odot}$) and stellar mass ($0.15 \times 10^6 M_{\odot}$), which could be a sign of the existence of large amounts of dark matter with a very low surface brightness of $\Sigma_V = 28.0 \pm 1.2$ mag arcsec⁻².

Different values have been reported for the distance modulus using two methods, the horizontal branch (HB) and the tip of the red giant branch (TRGB). In Table 2, we summarize the distance modulus calculated in other works. In this paper, we calculate a distance modulus of $(m - M) = 24.56^{+0.05}_{-0.15}$ mag using the TRGB method (see Section 5).

This paper is organized as follows. In Section 2, we present the photometry results of And IX. Section 3 deals with the study of the variable candidates and their amplitudes. The cross-correlation of the INT catalog with the *Spitzer*, WISE, and SDSS catalogs is discussed in Section 4. A description of the physical parameters of And IX is presented in Section 5. We focus on the estimation of the SFH based on the LPVs, specifically in And IX in Section 6. Estimation of the mass-loss rate by modelling the SEDs based on the dust of the LPVs is discussed in Section 7. Finally, a summary of this work is presented in Section 8.

2. PHOTOMETRY

Table 2. Distance modulus reported in the literature.

Distance modulus (mag)	Method	Reference
24.42 ± 0.07	TRGB	McConnachie et al. (2005)
24.48 ± 0.20	TRGB	Zucker et al. (2004)
24.33 ± 0.10	TRGB	Harbeck et al. (2005)
24.42 ± 0.39	TRGB	Collins et al. (2010)
24.4	HB	Collins et al. (2010)
$24.46^{+0.28}_{-0.15}$	TRGB, HST ^a	Weisz et al. (2019a)
$24.43^{+0.06}_{-0.03}$	HB, HST ^b	Weisz et al. (2019a)
$23.89^{+0.31}_{-0.08}$	TRGB, Ground ^c	Weisz et al. (2019a)

^aHST-based TRGB distance modulus^bHST-based HB distance modulus^cGround-based TRGB distance modulus

Nine observations were made from June 21, 2015, to October 6, 2017 (Table 3), to determine the photometric variability of the stars. The observations were made with the 2.5-m wide field camera (WFC) at INT in the Sloan i' , Harris V , and RGO I filters. The Sloan i' was used to observe the minimal effects of dust attenuation among the visible wavelengths in addition to the most significant magnitude differences of LPVs compared to other populations. The Harris V was also used to check the color, temperature, and radius. THELI (Transforming HEavenly Light into Image) pipeline was used to process each night's observations and create a comprehensive mosaic image by removing noises and tool errors (Saremi et al. 2020).

We performed photometric measurements of And IX using the DAOPHOT/ALLSTAR package (Stetson 1987) on a charge-coupled device (CCD). Because the CCD4 covered more than two half-light radii (~ 5 arcmin) of And IX, we focused our study on the CCD4 (11.26×22.55 arcmin²). DAOPHOT distinguished stars from background noise and measured stellar brightness by aperture photometry. To obtain a more accurate magnitude and astrometry, a point spread function (PSF) was created by selecting a number of isolated and unsaturated stars in each image. The PSF-fitting photometry was performed with the ALLSTAR by subtracting all stars in each image based on the constructed PSF model. The DAOMASTER combined the output of the ALLSTAR from multiple individual images. Individual images combined to create a master mosaic image of the galaxy by MONTAGE2. Simultaneous reduction of all images by PSF-fitting photometry was performed by ALLFRAME (Stetson 1994). The master image of CCD4 with a half-light radius (yellow circle) and two half-light radii (blue circle) of And IX are shown in Fig. 1. A total of 8653 stellar sources were detected in CCD4, of which ~ 4030 are within

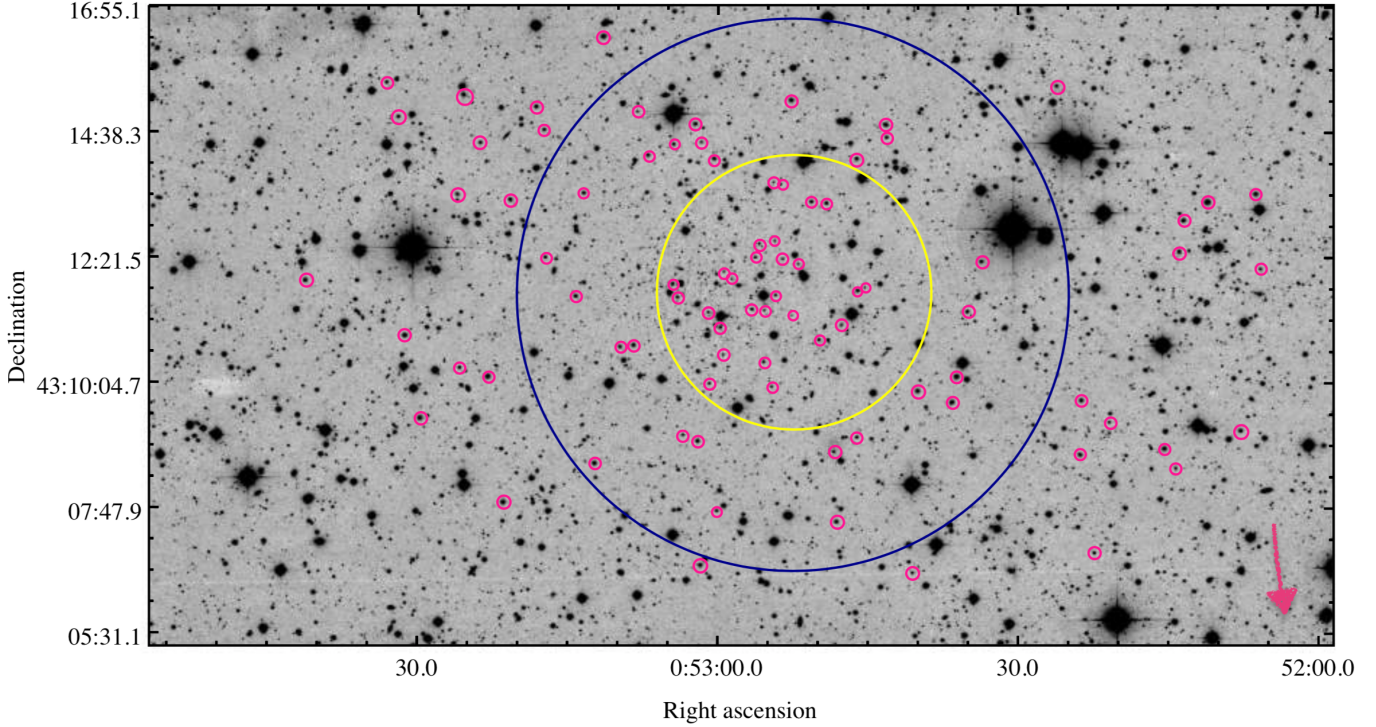


Figure 1. Montage of all frames of And IX dSph galaxy with variable candidates in pink circles. Half-light radius of ~ 2.5 arcmin (yellow circle) and two half-light radii (blue circle) of And IX are approximately noted. The pink arrow points toward the center of the M31 galaxy.

the two-half light radius. The photometric calibrations were performed as follows:

- Aperture correction: aperture growth curves were generated for a sample of stars (~ 40 bright and isolated stars) using the `DAOGROW` routine. The difference between the PSF-fitting and a large-aperture magnitude was derived from the `COLLECT` routine and added to all stellar sources using the `NEWTRIAL` routine (Stetson 1996, 1990).
- Zero point derivation: the transformation equations are derived by comparing Landolt standard stars and SDSS photometry based on the zero point and atmospheric extinction (Jordi et al. 2006). The average of the zero points is used for nights without a standard field. The transformation equations are applied by the `CCDAVE` routine and all images are calibrated with the `NEWTRIAL` (Stetson 1996).
- Relative calibration: we selected a sample of 1000 common stars in all images with magnitudes ranging from 17 to 21 mag. The mean magnitude was estimated at all epochs for each star, taking into account the photometric errors. We then applied the average value of the deviation of the mean magnitude of each star to all epochs. This step ensures that we have calibrated the magnitude of the LPVs. Fully described details of the

Table 3. Observations of And IX

Date (y m d)	Epoch	Filter	$t_{exp}(\text{sec})$	Airmass
2015 06 21	1	I	45	1.265
2015 06 21	1	V	72	1.253
2016 02 09	2	i	540	1.854
2016 06 15	3	i	555	1.409
2016 08 11	4	i	555	1.045
2016 08 13	4	V	735	1.033
2016 10 21	5	i	555	1.320
2017 01 29	6	i	435	1.655
2017 08 01	7	i	555	1.306
2017 08 01	7	V	735	1.227
2017 09 02	8	i	555	1.070
2017 09 02	8	V	735	1.047
2017 10 06	9	i	555	1.341

photometric procedure can be found in Saremi et al. (2020).

To investigate photometric completeness, we performed the `ADDSTAR` task in the `DAOPHOT` package. 1050 artificial stars in a range from 17 to 24 mag were added at random positions.

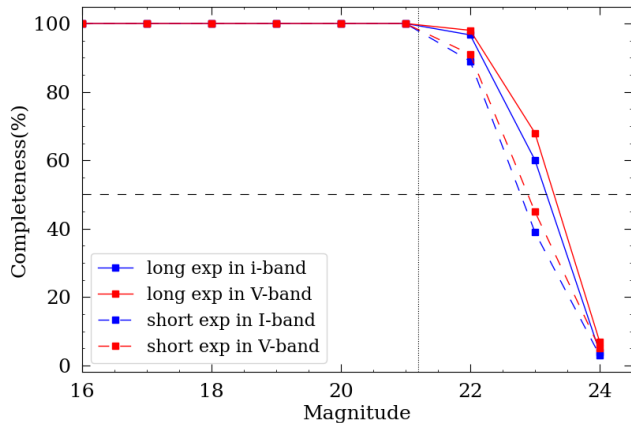


Figure 2. Completeness limit vs. magnitude for the long exposure times in the i -band (blue solid line) and in the V -band (red solid line). The short exposure times are also in the I -band (blue dashed line) and V -band (red dashed line). The dotted vertical line shows the tip of the RGB.

The completeness limits as a function of magnitude are shown for long and short exposure time images in the i -, I -, and V -bands in Fig. 2. The completeness limit is at 100% above the peak of the RGB around ~ 21.20 mag. The extracted catalog is more than 90% complete up to the ~ 22 mag for long exposure frames and more than 85% complete in frames taken in 2015. The completeness limit as a criterion of recovered stars has dropped to 50% for fainter stars (magnitude > 22.8 mag). The catalog covers all AGB stars in the observed region, as we search for AGB stars between the tip of the AGB at $i = 17.29$ mag and the tip of the RGB at $i = 21.20$ mag (see Section 5 for more information on how tips of the AGB and RGB are calculated). The magnitude differences between the recovered (output of photometry) and assigned magnitude (by ADDSTAR) of the artificial stars vs. magnitude in the i -band are shown in Fig. 3. These differences range from $-1 < \Delta i < 0.5$ mag. Despite the acceptable completeness in the I -band magnitude, we eliminated it in the later steps such as the search for variables and SFH. The calibration procedures were not applied to this filter because there was no transformation equation between the I -band magnitude and two other bands (refer to Section 4.3 for more details).

3. PROBING VARIABLE CANDIDATES

3.1. Evaluation of variables

One of the most reliable methods for determining variability in a sample of stars was introduced by Welch & Stetson (1993), which was further developed in Stetson (1996). The

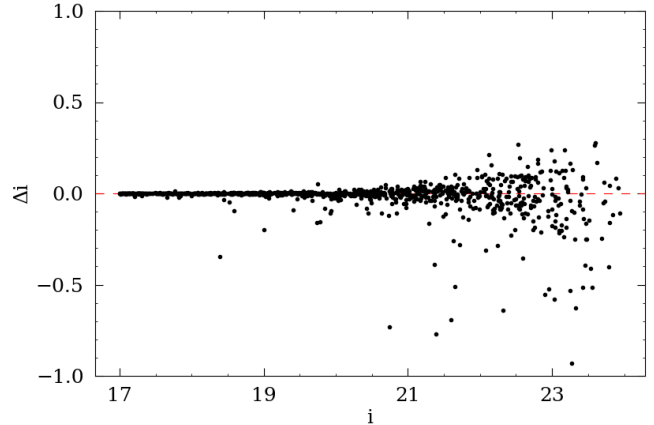


Figure 3. Differences between the recovered and assigned magnitude of artificial stars by ADDSTAR vs. magnitude in the i -band.

decisive variable index, L , is determined by combining two indexes J and K as follows:

$$L = \frac{J \times K}{0.798} \frac{\sum_{i=1}^n \omega_i}{\omega_{all}}. \quad (1)$$

With random noise, the index J scatters around zero and has a large positive value for variable stars. The shape of the light-curve is also influenced by the index K . If the time difference between two frames is closer than the period of variability, the weight of each star, ω_i , is equal to 1, whereas in a single frame, $\omega_i = 0.5$. $\sum \omega_i$ is the total weight assigned to a star based on the number of detections and ω_{all} is the total weight assigned to a star when it has been observed at all epochs.

Fig. 4 can be considered as a Gaussian function (red curve), mirrored around $L = 0$, with an excess at high L , representing statistically significant variable stars. We fit a Gaussian function to the negative distribution of L in each magnitude bin. If the number of stars in a given (positive) L and a given magnitude bin exceeds the Gaussian fit by a factor of 10 (indicating a 90% chance that it is a true variable), we set a threshold for candidate variability (vertical black dotted line). This threshold is indicated by the red dots in Fig. 5.

Fig. 5 shows a scatter plot of variability index L for different magnitude intervals. To detect variable candidates in all magnitude ranges, a polynomial function is fitted to the variability index threshold which varies with magnitude. A total of 411 variable candidates were detected over an area of about 0.07 deg^2 (\sim area of CCD4).

The accuracy of the variability index estimate was evaluated using the task ADDSTAR of the package DAOPHOT (Stetson 1987). In this way, 1200 artificial stars with magnitudes in the range of 16 – 22 mag were added to all frames in 6 steps

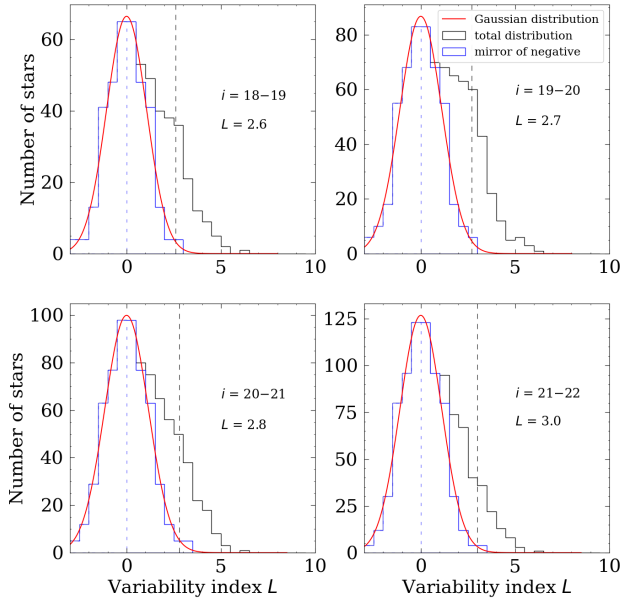


Figure 4. The red curves are the predicted Gaussian functions fitted to the histograms of variability indexes of And IX population. The blue dashed lines are with $L = 0$ and the negative part of the blue histograms ($L < 0$) are mirrored. Vertical black dashed lines represent the thresholds of the variability indexes in each magnitude bin.

with random positions and constant light-curves. Photometric procedures and assessment of variability index L for the synthetic population were performed as previously described. The distribution of the variability indexes of the artificial stars, based on their magnitude is overplotted in Fig. 5. It can be seen that no more than 1.16% of these artificial constant stars have a variability index above the threshold value, indicating a fairly reliable estimate of the threshold value.

Fig. 6 shows the light-curves of the variable candidates and a non-variable star to highlight the distinction between their light-curves. The magnitudes of the variable ones show remarkable changes around the mean magnitude (the first two plots), while the non-variable star (the third plot) shows only small changes in magnitude around its mean, shown by horizontal dashed lines. Variable candidates (the first two plots) were detected in *Spitzer* and SDSS surveys (Planck Collaboration et al. 2014; Boyer et al. 2015a). In addition to these surveys, WISE also discovered the candidate #5503 (Cutri et al. 2021). Table 6 provides more details about variable stars.

3.2. And IX Contamination

Foreground Milky Way contamination must be removed from And IX to distinguish dwarf galaxy stellar populations,

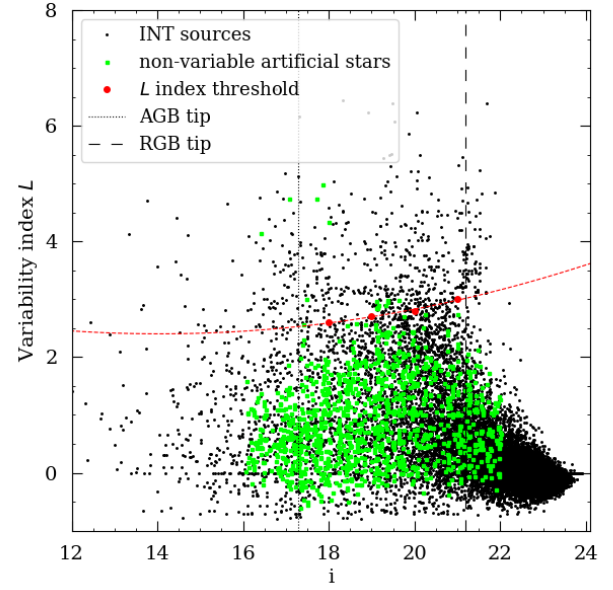


Figure 5. Distribution of variability indexes as a function of magnitude with the best fit of the polynomial function (red dashed line) to the indexes threshold in $i \in [18,19,20,21]$ mag. Variability indexes of artificial stars in the range of $16 \leq i \leq 22$ mag marked in green. The tips of the AGB and RGB are shown with vertical black lines at 17.29 and 21.20 mag, respectively.

especially before SFH are constructed from LPVs. To detect foreground contamination, we cross-correlated our catalog with *Gaia* Data Release 3 (DR3; (Gaia Collaboration et al. 2021)). We also considered TRILEGAL simulations of the Milky Way population to account for the level of contamination (Girardi et al. 2005). The *Gaia* sources in green are overplotted on the INT populations in the upper panels of Fig. 7. We included the entire field observed in CCD4 (0.07 deg², left panels of Fig. 7) and a region within a half-light radius (0.005 deg², right panels of Fig. 7). Populations of the Milky Way must either satisfy the proper motion criteria $\sqrt{(\mu_{RA})^2 + (\mu_{DEC})^2} > 0.28 \text{ mas yr}^{-1} + 2.0 \text{ error for } \mu$ as proper motion or $\text{Pa} / (\text{error of Pa}) \geq 2\sigma$ (Pa as parallax) (Saremi et al. 2020). Based on the adopted criteria, the total number of *Gaia* sources detected in our observation is estimated to be 890 in the region of CCD4 and 171 within the half-light radius of And IX. About 80% of the variable candidates in CCD4, $\sim 55\%$ in two half-light radii, and less than 27% within the half-light radius are detected by *Gaia* as foreground contamination. *Gaia*'s faint source limit is $G \sim 20.5$ mag and its completeness limit is $G \sim 17$ mag (Gaia Collaboration et al. 2021).

Foreground contamination of And IX is simulated using the TRILEGAL tool, at galactic coordinates $\ell = 123.212^\circ$, $b = -19.675^\circ$, and Galactic extinction $A_V = 0.206$ mag. The

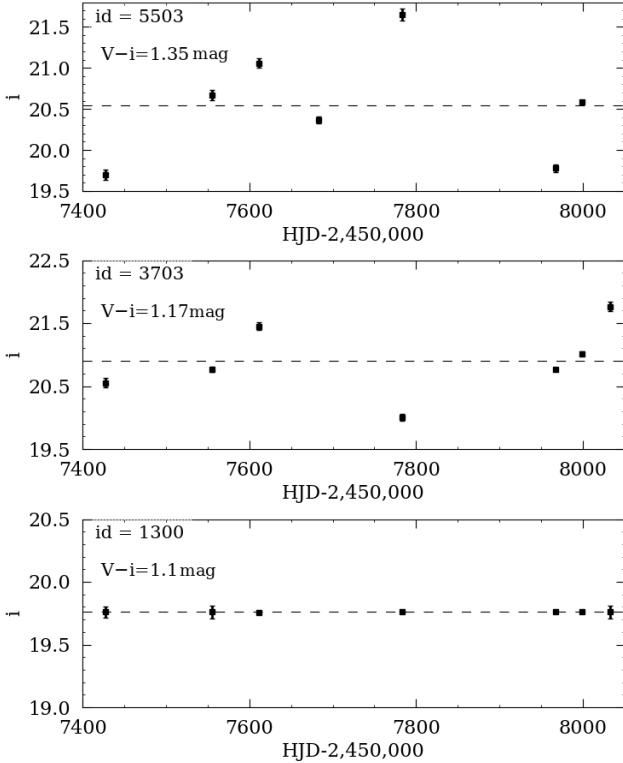


Figure 6. Examples of light-curves, two variable candidates in the first two plots, and a non-variable star in the third plot. Vertical error bars represent magnitude error.

stellar population predicted by TRILEGAL along the line of sight of And IX in two panels is shown in pink in the lower panels of Fig. 7. The synthetic stars predicted by TRILEGAL are 1990 in CCD4 and 190 within the half-light radius. There is additional foreground contamination from the TRILEGAL simulation within CCD4 and the half-light radius compared to *Gaia* DR3 due to the *Gaia* limitation in the detection of very faint stars ($\sim i = 20.5$ mag). Comparing the foreground contamination in the two regions in Fig. 7, we see that foreground stars have less impact on the half-light radius despite a large number of foreground stars in CCD4.

In addition to the foreground stars of the Milky Way, our sample could be contaminated by stars in the halo of M31 (due to its proximity to M31). A plausible contamination by a giant stellar stream in the northeast of M31 has been suggested based on the study of velocity dispersion in the SPLASH survey (Tollerud et al. 2012). In addition, And IX is located in a halo substructure known as the Triangulum-Andromeda (Tri-And) region, and stars in this region could represent possible contamination (Rocha-Pinto et al. 2004).

The distribution of LPVs as a function of color ($V - i$) is compared in two regions with the same area to reveal the degree of contamination by the M31 halo in Fig. 8. Contamination is estimated by comparing the population within two half-light radii (right panel) and outside of the three half-light

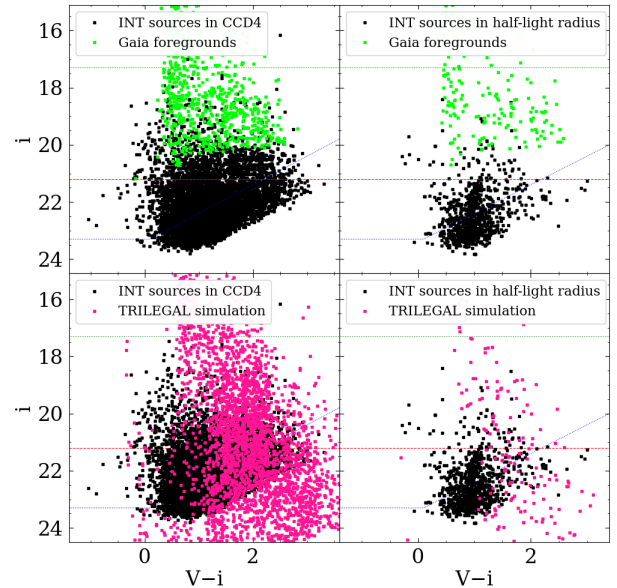


Figure 7. *Gaia* sources (in green) and TRILEGAL simulation of foreground contamination (in pink) are presented as a function of color. Stellar population confined in a field of ~ 0.07 deg² (area of CCD4) in the left panels, and in ~ 0.005 deg² corresponding to the half-light radius in the right panels. Tips of the AGB and RGB are marked in green and red dashed lines, respectively. The completeness limit of our photometry is marked in blue.

radii (left panel). About 28% of the stellar population and 13% of the LPV candidates within two half-light radii are estimated as background contamination. Possibly they are stars in M31 and/or background active galactic nuclei (AGN) and/or foregrounds that are below *Gaia*'s limit of completeness. Fig. 8, left panel, shows no clear, curved RGB in the control field, suggesting that M31 contamination is negligible and most of the contamination comes from the Galactic foreground. It is noted that background galaxies and AGN contamination mainly affect the region around $V - i \sim 2$ mag and $i \gtrsim 21.5$ mag, not much affecting the AGB (or RGB) portion of the And IX CMD. In the following, foreground contamination of *Gaia* is excluded from the And IX population.

3.3. Amplitude of variable candidates

The shape of the light-curve is assumed to be sinusoidal to evaluate the amplitude of variability. The light-curves of the variable candidates in Fig. 6 are considered as examples in our data that show sinusoidal variability due to pulsations (blue signs in Fig. 9). Considering a value of 0.707 for the standard deviation of the unit sine function and a standard

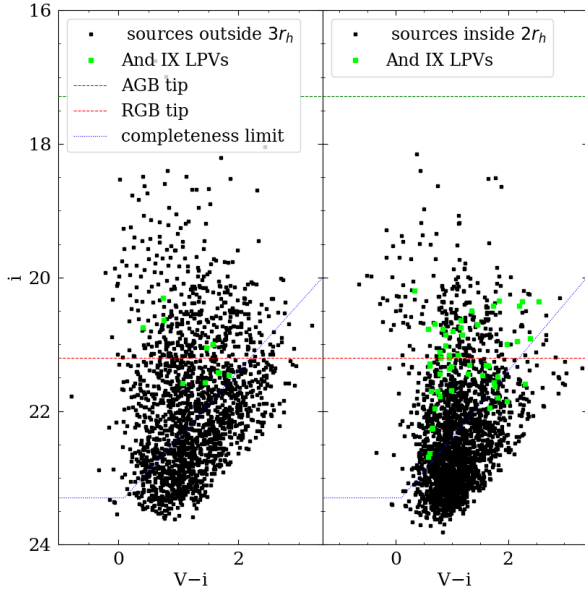


Figure 8. CMDs of And IX in the i vs. $V - i$ color showing our identified LPV candidates in green for two regions of a similar area within two half-light radii (right panel) and outside three half-light radii (left panel).

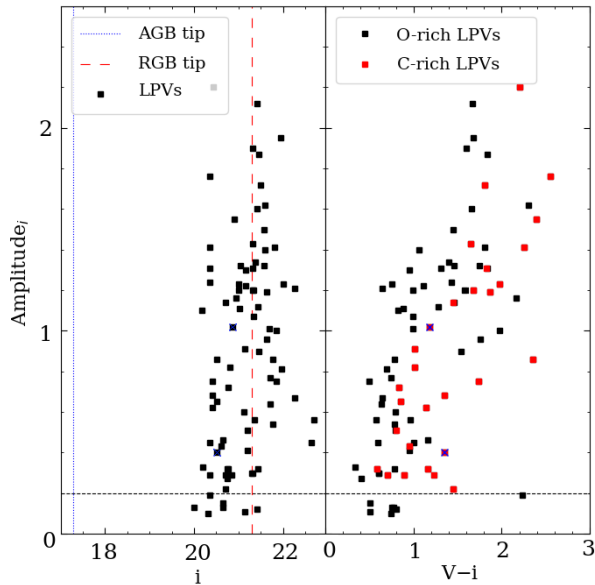


Figure 9. Amplitude of variability vs. magnitude in the i -band (left panel) and vs. color (right panel). Vertical blue and red dashed lines represent the tips of the AGB and RGB, respectively. 0.2 mag amplitude (horizontal black dashed line) is the threshold for distinguishing LPVs from other candidates.

deviation in our data, σ (Javadi et al. 2011a), the amplitude is estimated by:

$$\text{Amplitude} = \frac{2 \times \sigma}{0.707}. \quad (2)$$

The amplitude of the variable candidates in the range 0.1 – 2.20 mag, as a function of magnitude in the i -band, is shown in the left panel of Fig. 9. The horizontal black dashed line (0.2 mag) illustrates the LPV amplitude threshold (Saremi et al. 2020), and the blue dotted and red dashed lines are the tips of the AGB and RGB, respectively (see Section 5). It can be seen that LPV stars with larger amplitudes tend to be redder than those with smaller amplitudes. The right panel of Fig. 9 shows the amplitude in the i -band as a function of $(V - i)$ color. The amplitude almost increases with color for more candidates. The stars become redder and fainter as they evolve in the giant star branch. During the evolution of stars along the AGB, they become more luminous, so dust must attenuate their light if they appear fainter. Additionally, the amplitude of the variability increases in the AGB phase as they evolve (Wood et al. 1992; McDonald & Zijlstra 2016; McDonald & Trabucchi 2019). The larger amplitude can be explained by the lower luminosity of lower-mass AGB stars; thus, RSGs typically have a lower amplitude (Wood et al. 1992; Wood 1998; Whitelock et al. 2003; van Loon et al. 2008).

C-rich variable candidates of the INT survey which are classified on the basis of birth mass (see Section 6), are shown in red squares in the right panel of Fig. 9. The amplitudes of this sample almost increase with increasing reddening, just as in the *Spitzer* observations of C-rich variables in LMC and IC 1631 (Whitelock et al. 2017). Dust-enshrouded variables that have larger amplitudes experience more mass-loss and become redder (Whitelock et al. 1991). As well, O-rich variable candidates in the INT survey (black squares in the right panel of Fig. 9) with a redder color have a larger amplitude.

A total of seven stars with amplitudes less than 0.2 mag in the i -band in CCD4 and four within two half-light radii were excluded from the variability analysis. The LPVs have variability amplitudes greater than 0.2 mag, and we are also unsure of the nature of the variable candidates with amplitudes less than 0.2 mag.

4. CROSS-MATCH WITH OTHER CATALOGS

4.1. *Spitzer* catalog cross-identification

A cross-correlation was carried out between the And IX INT catalog and mid-IR data from the *Spitzer* Space Telescope, IRAC, in 3.6- and 4.5- μm bands as part of the DUSTiNGS survey (DUST in Nearby Galaxies with *Spitzer*) (Boyer et al. 2015a). The two catalogs have 1638 common sources within two half-light radii of the center, out of which 50 ($\sim 3\%$) are INT LPV candidates. DUSTiNGS reported five ex-

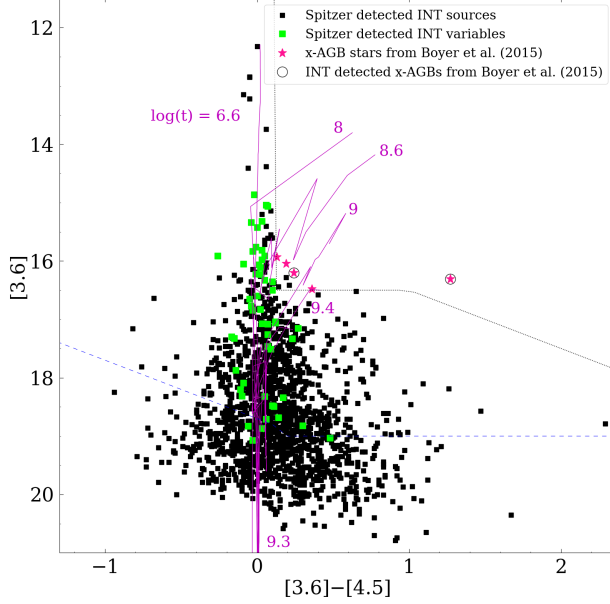


Figure 10. CMD of *Spitzer* detected INT sources. *Spitzer* detected LPVs are highlighted in green squares, and PADOVA isochrones from [Marigo et al. \(2017\)](#) are marked in magenta. The blue dashed line represents the 75% completeness limit of *Spitzer* data, and the dotted black line separates the plausible region of x-AGB stars ([Boyer et al. 2015b](#)).

trema AGB (x-AGB) candidates ([Boyer et al. 2015b](#)), only two detected in our survey (black open circles in Fig. 10) as LPV candidates (#5671 and #4433) and two others as non-variable population (#3770 and #5025). As in [Boyer et al. \(2015b\)](#) explained because of imaging artifacts some stars may appear artificially variable in their survey. We estimated the variability index of these two non-variable stars less than the variability threshold in their magnitude range and also their light-curves do not show apparent variability. Our survey did not observe the last one because it is located outside CCD4; therefore, it is unlikely to be And IX’s population, as it lies outside the two half-light radii. In [Goldman et al. \(2019\)](#), just one of these LPV candidates was introduced with clear variability. This x-AGB (#5671) is also detected in our survey within the half-light radius of And IX. According to [Goldman et al. \(2019\)](#), this candidate has a period of 467 days and an amplitude of 0.8 mag. There is also a huge difference in color between it and the rest of the x-AGBs, with a color of $[3.6] - [4.5] = 1.26$ mag, in Fig. 10. Two x-AGBs sources detected as LPVs in our survey with sinusoidal fits are presented in Fig. 11, along with their mass-loss rate (\dot{M}) (see Section 7.2) and amplitude in the *i*-band (amplitude_{*i*}) based on our calculations. In our estimation, LPVs #5671 and #4433 have

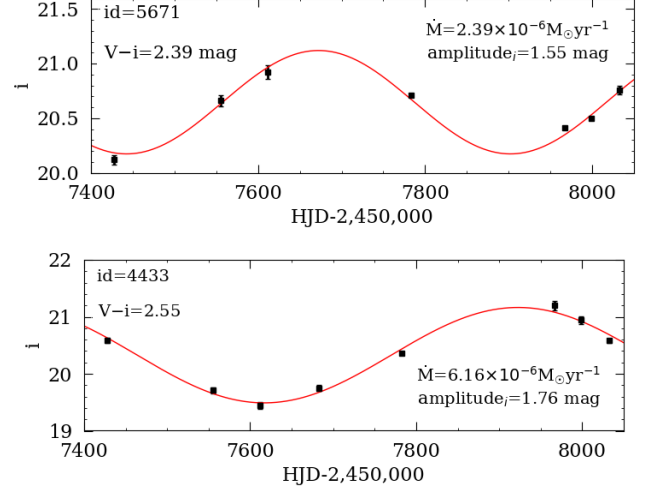


Figure 11. Two light-curves of mutual x-AGBs in INT and the DUSTiNGS catalog of variable *Spitzer* sources ([Boyer et al. 2015b](#)) with sinusoidal fits in red curves.

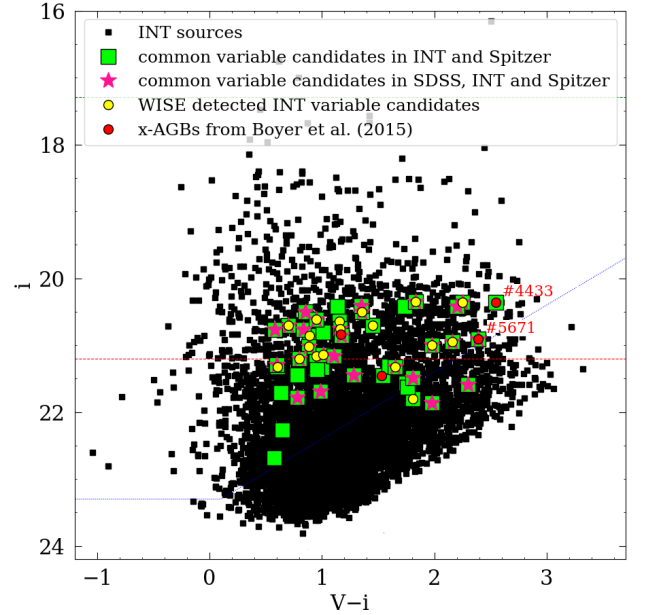


Figure 12. CMD of mutual sources from the INT, *Spitzer*, WISE, and SDSS surveys within two half-light radii of And IX. Four x-AGBs from [Boyer et al. \(2015b\)](#) are marked with red circles. The AGB-tip and RGB-tip are illustrated by the green and red dashed lines, respectively. The blue dashed line represents the estimated completeness limit. #5561 and #4433 are mutual x-AGBs between the INT and the *Spitzer*.

periods of 530 (which is very close to [Goldman et al. \(2019\)](#)’s estimate of 467 days) and 585 days.

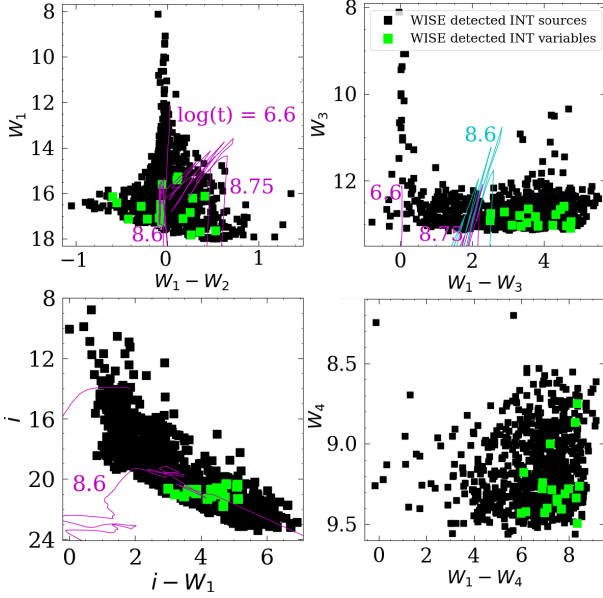


Figure 13. CMD of mutual sources from INT and WISE surveys. Green squares represent mutual LPVs between INT and WISE. The Padova isochrones (Marigo et al. 2017) are also marked in magenta and blue.

4.2. WISE catalog cross-identifications

The WISE (Wide-field Infrared Survey Explorer) ALL-SKY data release 2013 (Cutri et al. 2021) in $W_1 = 3.35$, $W_2 = 4.60$, $W_3 = 11.56$, and $W_4 = 22.09$ μm bands was cross-correlated with the INT catalog of And IX. A total of 864 stellar sources are identified between the INT and the WISE, of which 19 are among the INT variable candidates. The mutual LPVs between the INT and the WISE are low because most of them are in dense regions where we do not get any WISE matches because of the limited angular resolution of WISE. Fig. 12 shows a comprehensive CMD of the And IX population with common LPVs in INT, *Spitzer*, WISE, and SDSS. Matched LPVs between WISE and INT are marked with yellow circles. Fig. 13 shows the mutual stars of the WISE and INT surveys in four subplots. The *Spitzer* and SDSS surveys have a better photometric quality than WISE and have more stars in common with the INT survey. According to the SEDs (Fig. 28), the W_4 and some W_3 data are too bright compared to the other bands. A poor spatial resolution (6.5" and 12.0" for W_3 and W_4 , respectively) could have contributed to this.

4.3. SDSS catalog cross-identifications

We cross-matched the INT catalog with the SDSS data release 12 (DR12) (Planck Collaboration et al. 2014), the last data released from SDSS-III, in five bands u , g , r , i , and z from 2008 to 2014. The number of common sources between the SDSS catalog and master catalog of And IX is ~ 2680 , of

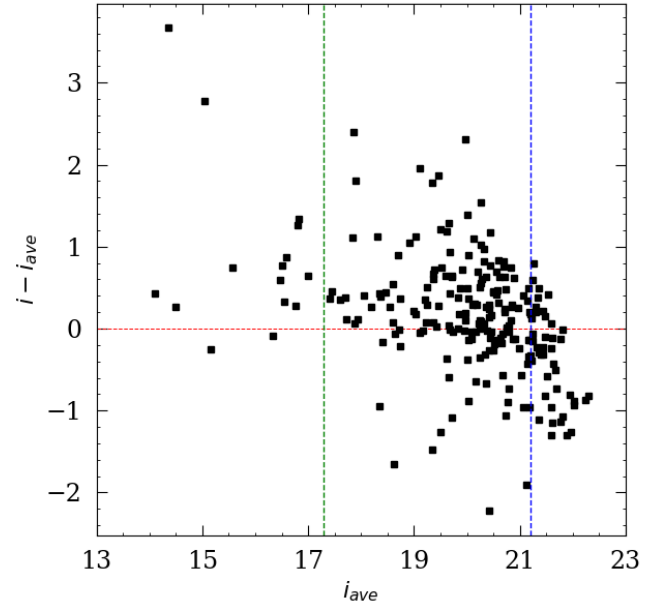


Figure 14. The difference of the calculated magnitude in the Sloan i filter based on the transformation equation (Jordi et al. 2006) with the average magnitude of all frames except 21 Oct *vs.* average magnitude for non-variable stars. The tips of the AGB and RGB are shown with vertical green and blue lines at 17.29 and 21.20 mag, respectively.

which 27 are LPVs. More than 80% of matched sources have magnitude differences less than $\Delta i < 1$ mag, as we used SDSS photometry to transform our magnitude to the photometric standard system (Landolt). *Spitzer* data are available for all 27 LPVs that are mutual between the SDSS and INT (pink stars in Fig. 12).

In the INT survey, an observation was made on 21 October in Landolt I filter. The transformation equation (Jordi et al. 2006) must be used to convert Landolt I filter to Sloan i filter for the 230 mutual stars between the SDSS catalog and frame in Landolt I filter, but since we do not have color in the Landolt system, we use the color ($i - z$) in the SDSS catalog which has observation in Landolt I filter. Due to the short exposure time of this frame (Table 3), fewer stars were identified than between the master catalog and the SDSS catalog. Fig. 14 shows the difference of the magnitude in the Sloan i filter on 21 October with the average magnitude (i_{ave}) in all observation (except 21 October) frames for non-variable stars *vs.* the average magnitude.

There is a large scatter for the magnitude range of interest (between RGB-tip and AGB-tip), which makes the filter transformation inaccurate. As a further illustration, in Fig. 15, we plot the magnitude differences between the SDSS and INT catalogs ($i_{INT} - i_{SDSS}$ *vs.* i_{INT}). The magnitude difference between the two surveys is distributed around zero,

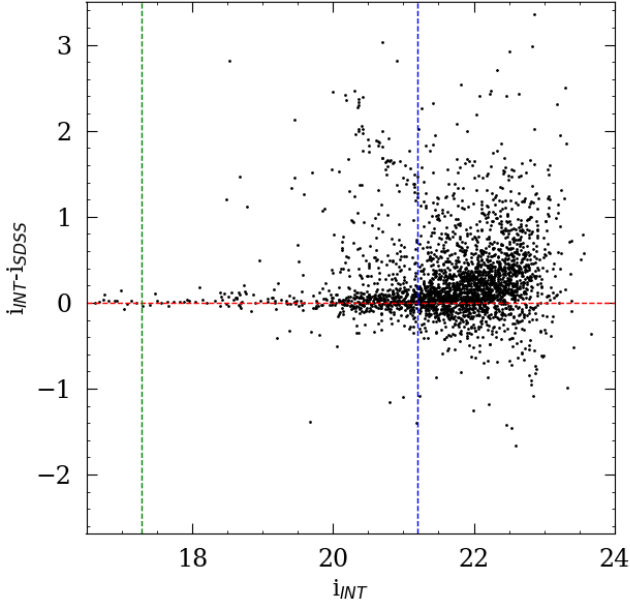


Figure 15. Magnitude differences between INT catalog and SDSS of And IX, plotted against i magnitude of our catalog. The tips of the AGB and RGB are shown with vertical green and blue lines at 17.29 and 21.20 mag, respectively.

which indicates the accuracy of magnitude calibration, but the scatter is still quite large. As a result, SDSS colors cannot be used in transformation equations to estimate i -band magnitudes for LPV identification which requires high accuracy in magnitude estimation of any epoch.

5. SURVEYING PHYSICAL PARAMETERS OF AND IX

We have presented And IX stellar density profile (in pink) and surface brightness (mag arcsec^{-2}) (in black) as a function of distance from the galaxy center in Fig. 16. A half-light radius of 2.50 ± 0.26 arcmin (597_{-67}^{+62} pc) results from the calculation of the half area under the most optimal exponential fit (blue curve) to the number density and surface brightness data. Our calculation agreed well with the [McConnachie \(2012\)](#) estimate of about 2.5 ± 0.1 arcmin. In addition, radii of 2.5 ± 0.1 , 2.6 ± 0.1 , and 2.7 ± 0.2 arcmin were estimated for the half-light radius by [Collins et al. \(2010\)](#) considering the best fit of the exponential, Plummer, and King models, respectively, to the distribution of number density as a function of radius.

The magnitude of the tip of the RGB, as a distance indicator, has been used to estimate the distance of the galaxy ([Lee et al. 1993](#)). On reaching the end of the RGB, stars ignite helium in their cores. At the tip of the RGB, stars reach maximum luminosity through helium flashes. The TRGB magnitude in the I -band has the least dependence on a star's age and chemistry, making it the most reliable magnitude to use as a standard candle ([Lee et al. 1993](#)). It was not

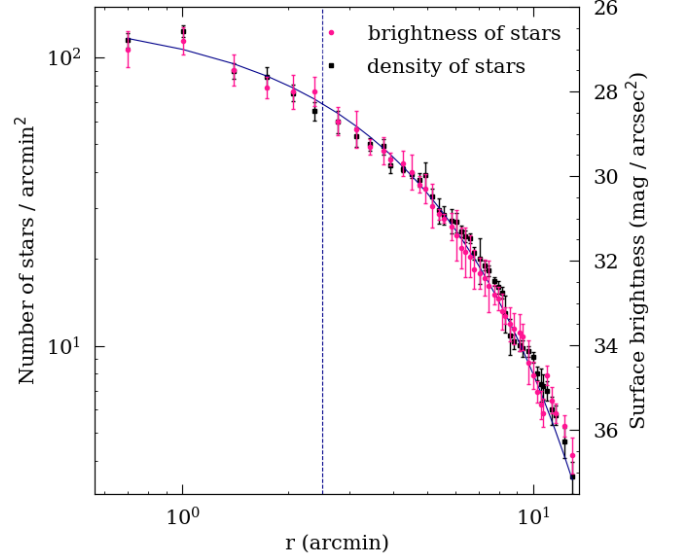


Figure 16. The stellar number density and surface brightness of And IX with the best exponential fit to the data (blue curve) as a function of galactocentric distance. The blue dashed line represents the half-light radius (2.50 ± 0.26 arcmin). The vertical error bar results from the Poisson uncertainty of the counts.

possible to convert the photometry bands to I -band using the transformation equations in [Lupton \(2005\)](#) via the Johnson-Cousins system due to the lack of a third filter. Therefore, we calculated the TRGB magnitude in the i -band.

A population of stellar sources in an area within two half-light radii (~ 0.022 deg 2) is selected to estimate the distance of the galaxy, as used in [McConnachie et al. \(2004\)](#). This region is located between two pink lines (left panel in Fig. 17) of $0.28 < V - i < 1.07$ mag and $18.51 < i < 23.81$ mag to isolate the populations in the red giant branch. The magnitude of the TRGB can be calculated by constructing the i -band luminosity distribution as a binned histogram with 0.05 mag (middle panel in Fig. 17). By convolving the smooth luminosity function with the summation of the normalized Gaussian distribution ([Sakai et al. 1996](#)) through a Sobel edge kernel $[-2, -1, 0, +1, +2]$, the position of the tip of the RGB at which the convolution is maximum is determined (right panel in Fig. 17) ([Lee et al. 1993](#)).

The distance modulus of $24.56_{-0.15}^{+0.05}$ mag ($\sim 816.58_{-54.50}^{+19.02}$ kpc) results from the tip of the RGB at $i = 21.20_{-0.15}^{+0.05}$ mag (highlighted in purple in Fig. 17). In this derivation, a correction of $2.086 \times E(B - V)$ with 0.075 mag as reddening ([Schlegel et al. 1998](#)) is used for the Galactic extinction in i -band. Also, we adopt an absolute magnitude of -3.52 mag for the tip of the RGB in the i -band based on the PARSEC isochrones in the SDSS photometry system ([Bressan et al. 2012](#)). Estimates of the distance modulus to And IX vary

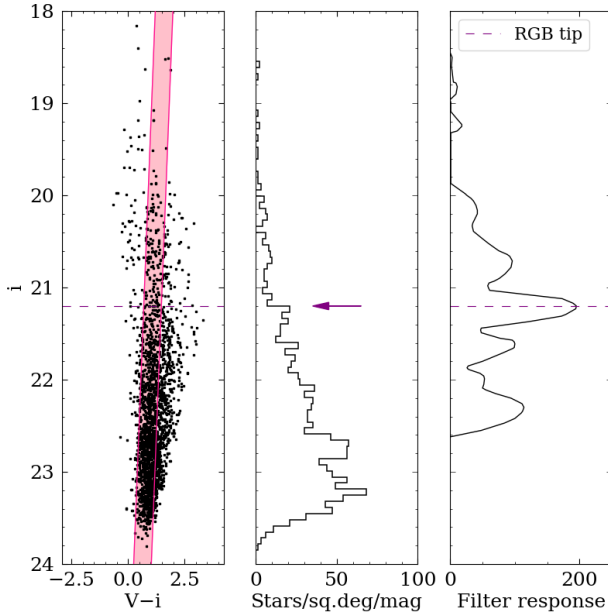


Figure 17. The left panel shows And IX sources in two half-light radii. The middle panel represents the histogram of the luminosity function. The right panel shows the Sobel filter response for the tip of the RGB with edge detection. The tip of the RGB is detected at $i = 21.20^{+0.05}_{-0.15}$ mag and marked on the CMD by a horizontal purple dotted line and on the luminosity functions by an arrow.

from $23.89^{+0.31}_{-0.08}$ mag (Weisz et al. 2019a) to 24.42 ± 0.39 mag (Collins et al. 2010).

CMD of the stellar population of And IX within two half-light radii (~ 5 arcmin) is shown in Fig. 18. All LPV candidates and those with amplitude $i < 0.2$ mag are marked in green and orange squares, respectively. The spatial distribution of variable candidates within two half-light radii is shown in pink circles in Fig. 1. The overlaid Padova¹ stellar evolutionary tracks illustrated in magenta, range from ~ 31.62 Myr to 10 Gyr (Marigo et al. 2017). A distance modulus of $24.56^{+0.05}_{-0.15}$ mag and metallicity $Z = 0.0001$ are used for all stellar tracks in this paper. A total of 8653 stellar sources and 84 variable candidates were detected in an area of 11.26×22.55 arcmin² (2.69×5.39 kpc²), which corresponds to the CCD4 of the WFC.

AGB stars at the tip of the AGB are optically obscured by dust due to high mass-loss. The Chandrasekhar core mass for the classical AGB limit is obtained in $M_{bol} = 7.1$ mag ($M_{bol} < -8$ mag for supergiants) considering the classical core luminosity relation (Zijlstra et al. 1996). From Padova evolutionary model, the classical AGB limit is estimated to

¹ <http://stev.oapd.inaf.it>

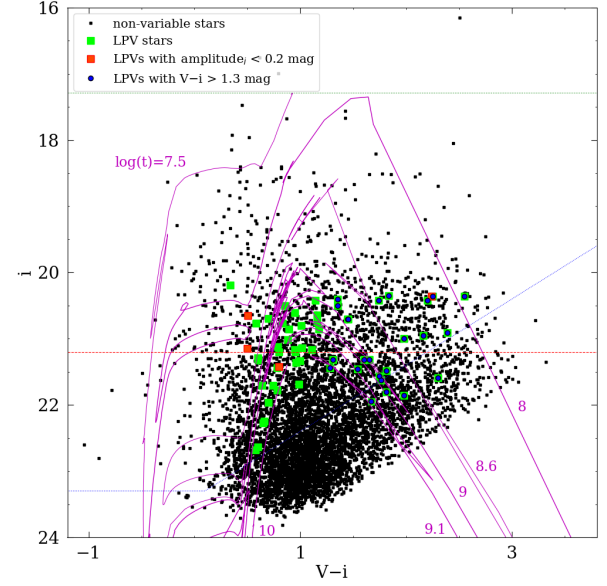


Figure 18. CMD of And IX sources in an area within two half-light radii. The variable candidates are marked with green squares and those with amplitude $i < 0.2$ mag with orange squares. The completeness limit of the photometry (blue), the AGB-tip (green), and the RGB-tip (red) are shown in the graph. The Padova isochrones (Marigo et al. 2017) are also marked in magenta. Dust correction will be applied to the LPVs shown in blue.

be $\log(t) = 7.5$ ($t = 31.62$ Myr) for the tip of the AGB (green dashed line) with $i = 17.29$ mag. Fig. 18 also shows a red dashed line representing the tip of the RGB at $i = 21.20$ mag, and the completeness limit of the photometry in blue.

6. FROM VARIABLE CANDIDATES TO STAR FORMATION HISTORY

As mentioned, to reconstruct the SFH of And IX we will use the candidates of LPVs, since there is a relation between their luminosity and their birth mass. This is possible by Padova stellar evolutionary tracks which link the luminosity of LPVs to their birth mass. The Padova tracks are a comprehensive description of stellar evolution from the first thermal pulse of the AGBs to the post-AGB phase. The effects of circumstellar extinction and different chemical composition of dust are also considered (Marigo et al. 2017). The age and pulsation duration of LPVs are derived from the birth mass-age and birth mass-pulsation duration relationships. Suitable coefficients for these relations with a distance modulus of $24.56^{+0.05}_{-0.15}$ mag and metallicities of $Z = 0.0001$, $Z = 0.0002$, and $Z = 0.0003$ were derived by Saremi et al. (2021).

As AGB stars evolve, their bolometric luminosity should increase, but as they become cooler and more dust-enshrouded, their optical brightness will decrease. In other words, AGB

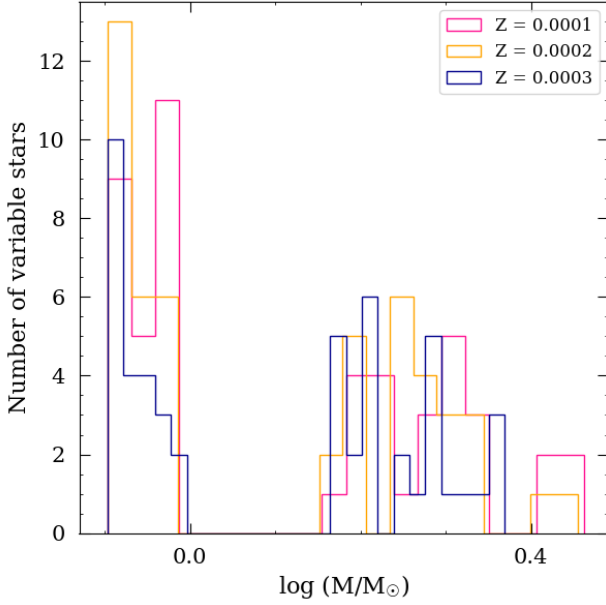


Figure 19. The histogram of the number of variable stars within two half-light radii in metallicities $Z = 0.0001$ (pink), $Z = 0.0002$ (orange), and $Z = 0.0003$ (blue).

stars re-emit the absorbed IR radiation at larger wavelengths. The AGB stars become fainter and redder due to extinction, both from interstellar dust and circumstellar dust. It is therefore necessary to apply a magnitude correction to stars enveloped by dust in addition to the Galactic extinction correction.

We have a magnitude correction for the LPVs with $V - i > 1.3$ mag to bring them back to $V - i = 1$ mag. The slopes of the isochrones for O-rich evolutionary tracks tend to redden faster compared to C-rich tracks. In our sample, O-rich and C-rich stars have average slopes of 3.31 and 2.37 mag mag⁻¹, respectively. The calculations were performed using the isochrones from Fig. 18. Blue points in Fig. 18 indicate LPV candidates affected by circumstellar dust, so the magnitude correction will be applied. The correction equation with "a" as the slope of the isochrones is:

$$i_0 = i + a[(V - i)_0 - (V - i)] \quad (3)$$

First, a carbon correction equation is applied to our sample by assuming that our LPVs are C-rich. The birth mass is derived using the corrected magnitude in the i -band and the relation between birth mass and luminosity. This assumption is correct if $1.5 \leq M/M_\odot \leq 4$ (Saremi et al. 2021). Otherwise, our sample should be de-reddened by the oxygen correction equation (see Section 7 for more details on the mass range). The histogram in Fig. 19 shows the number of variable stars in different mass ranges for three metallicities.

There are no variable stars with a mass of 1-1.5 M_\odot in this galaxy, according to the histogram.

6.1. Calculation method for star formation rate

Based on the mass, age, and pulsation duration of the LPVs, the star formation rate (SFR) is calculated. We use the mass-luminosity relation to convert the i -band magnitudes of the LPV stars to their masses. There is a correlation between the most luminous point in each isochron and its associated mass. Using a function fitted to all points derived from different isochrones, constant coefficients can be obtained for different luminosity intervals at different magnitude intervals to calculate the birth mass. Here, we used the coefficients of the best fit of the function reported by Saremi et al. (2021) to derive the relationships between mass and luminosity, mass and age, and mass and pulsation duration.

The SFR, $\xi(t)$ ($M_\odot \text{ yr}^{-1}$), as a function of time, is used to derive the SFH. The method used in this paper was adapted from Javadi et al. (2011b, 2017); Hamedani Golshan et al. (2017), and has also been used to reconstruct the SFH of other dwarf galaxies in the Local Group by Rezaeikh et al. (2014); Hamedani Golshan et al. (2017); Hashemi et al. (2019); Saremi et al. (2021); Navabi et al. (2021); Parto et al. (2023). In this method, the SFR is derived based on the initial mass function (IMF) of Kroupa (2001) to describe the initial mass distribution of stars, rather than the number of stars. The SFR is calculated by considering the LPV mass in the range from $m(t)$ to $m(t + dt)$, δt as the pulsation duration (the total amount of time a star is a LPV), and dn' as the number of stars in each period. The SFR is given by:

$$\xi(t) = \frac{dn'(t)}{\delta t} \frac{\int_{m(t)}^{m(t+dt)} f_{IMF}(m)m dm}{\int_{m(t)}^{m(t+dt)} f_{IMF}(m)dm} \quad (4)$$

Massive stars evolve more quickly, and their pulsating phases last only a short time. However, low-mass stars spend more time in this phase and are more likely to appear in the pulsation phase. So we use pulsation duration in this formula as a correction factor. By considering a Poisson statistic distribution of the number of stars in each bin as N , the statistical error is calculated as,

$$\sigma = \frac{\sqrt{N}}{N} \xi(t) \quad (5)$$

6.2. The star formation history in And IX

The birth mass, age, and pulsation duration are calculated from the brightness of LPVs. Stars are sorted by mass and classified into bins with the same number of stars, so the mass span in each interval is specified for IMF integration.

Metallicity is an important factor in stellar evolutionary tracks, so it could affect the determined SFH as well. Ac-

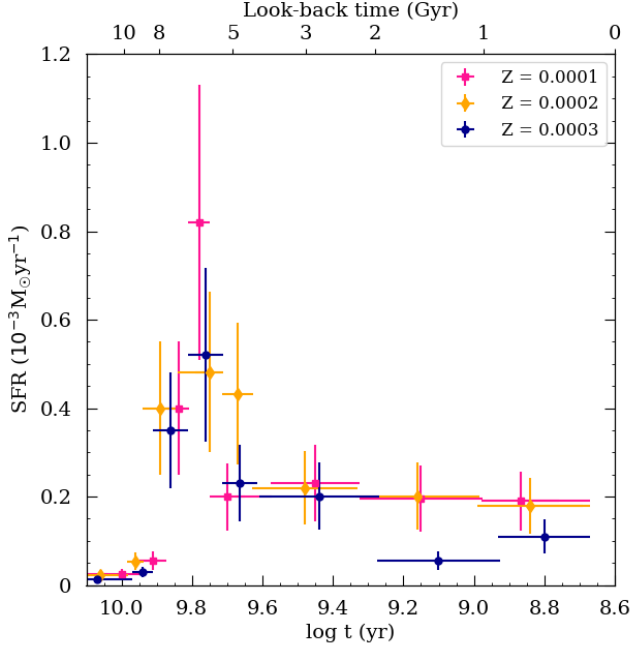


Figure 20. SFHs of And IX for metallicities of $Z = 0.0001$ (pink), $Z = 0.0002$ (orange), and $Z = 0.0003$ (blue) within two half-light radii ($\sim 0.022 \text{ deg}^2$).

According to the estimates, And IX’s metallicity is $[\text{Fe}/\text{H}] = -2.2 \pm 0.2 \text{ dex}$ ($\sim Z = 0.0001$) in Collins et al. (2010); McConnachie (2012), and also Wojno et al. (2020) calculated metallicity $[\text{Fe}/\text{H}] = -2.03 \pm 0.01 \text{ dex}$ ($\sim Z = 0.0002$). Kirby et al. (2013) reported a mean metallicity $[\text{Fe}/\text{H}] = -1.93 \pm 0.20 \text{ dex}$ ($\sim Z = 0.0002$), assuming a solar abundance of $12 + \log(\text{Fe}/\text{H}) = 7.52$. The metallicity of galaxies varies during their evolution, so in this study, we consider metallicity $Z = 0.0002$ as well as a more metal-rich estimate $Z = 0.0003$ in addition to the main metallicity $Z = 0.0001$.

Fig. 20 illustrates SFH in two half-light radii corresponding to metallicities $Z = 0.0001$, $Z = 0.0002$, and $Z = 0.0003$. Each age bin length and the statistical error on the SFR are represented by horizontal and vertical error bars, respectively. In this paper, we use the Λ CDM standard model with the cosmological parameters, the Hubble constant $H_0 = 67.3 \pm 1.2 \text{ km s}^{-1} \text{ Mpc}^{-1}$, the matter density parameter $\Omega_m = 0.315 \pm 0.017$, and the physical densities of baryons and cold dark matter $\Omega_b h^2 = 0.02205 \pm 0.00028$ and $\Omega_c h^2 = 0.1199 \pm 0.0027$, respectively, to calculate the redshift (Planck Collaboration et al. 2014).

The star formation epochs occurred between 500 Myr ($\log t = 8.67$) and 13 Gyr ago ($\log t = 10.1$). Assuming $Z = 0.0001$, the SFR reached a maximum of $8.2 \pm 3.1 \times 10^{-4} \text{ M}_\odot \text{ yr}^{-1}$ in 6 Gyr ago. During this period, SFR peaked at $4.8 \pm 1.8 \times 10^{-4} \text{ M}_\odot \text{ yr}^{-1}$ and $5.2 \pm 2.0 \times 10^{-4} \text{ M}_\odot \text{ yr}^{-1}$ for metallicities $Z = 0.0002$ and $Z = 0.0003$, respectively.

Comparing the SFRs in different metallicities show that $Z = 0.0001$ produces the highest peak of SFR due to its more metal-poor environment. Generally, the SFR decreases with increasing metallicity except for 1.41, 5.01, and 6.02 Gyr. SFR distributions for metallicities of $Z = 0.0001$ and $Z = 0.0003$ are used for this comparison. Unlike two other metallicities, the SFR at $Z = 0.0003$ peaks at 630 Myr ago (corresponding the errors, 850–457 Myr ago) with a rate of $11.0 \pm 4.0 \times 10^{-5} \text{ M}_\odot \text{ yr}^{-1}$.

Cross-correlation with the Boyer et al. (2015b) catalog of extreme AGB (x-AGB) stars provided the detection of two x-AGBs. Based on Boyer et al. (2015a) classification, x-AGB stars are variables with $M_{3,6} < 8 \text{ mag}$ and colors $[3.6] - [4.5] > 0.1 \text{ mag}$. They produce more than 75% of the dust produced by cool evolved stars, but they represent less than 6% of the total population of AGBs (Boyer et al. 2012). Two stars with masses exceeding 1.5 M_\odot and an estimated 1 Gyr to 1.58 Gyr of age have been identified as carbon stars. As a result of the existence of these C-rich AGB stars, there is a possibility that other C-rich AGBs are responsible for the revival of SFH. Also, these two carbon stars may be older AGBs that going through the bright part of their thermal-pulse cycle. However, more research is necessary to determine if dusty LPV mass-loss has recently increased SFR.

A total stellar mass over a specified time is calculated by aggregating $\xi(t)$ over that period. A total stellar mass of $3.0 \times 10^5 \text{ M}_\odot$ obtained for a metallicity of $Z = 0.0001$ within two half-light radii. In And IX, stellar mass is reduced by 20% ($\sim 2.4 \times 10^5 \text{ M}_\odot$) and 23% ($\sim 2.3 \times 10^5 \text{ M}_\odot$), in metallicities of $Z = 0.0002$ and $Z = 0.0003$, respectively. This study observed a decrease in total stellar mass due to increasing metallicity. Considering a metallicity of $[\text{Fe}/\text{H}] = -2.03 \pm 0.01$ ($\sim Z = 0.0002$), Wojno et al. (2020) estimated a stellar mass of $\sim 2.4 \times 10^5 \text{ M}_\odot$ ($\log(M/M_\odot) = 5.38 \pm 0.44$). According to the paper mentioned, the estimated stellar mass is similar.

While changing the distance modulus and Galactic extinction do not affect the age–mass, and pulsation–duration–mass relations, it will change the magnitude of LPV stars and hence their mass and the SFH of the galaxy. Fig. 21 and Fig. 22 are plotted separately in order to illustrate the potential differences between the effect of the distance modulus and Galactic extinction on SFRs. A comparison of the SFHs of And IX for distance modulus derived in this paper ($24.56^{+0.05}_{-0.15} \text{ mag}$) and the lowest distance modulus reported ($23.89^{+0.31}_{-0.08} \text{ mag}$ (Weisz et al. 2019a)) is shown in Fig. 21. As can be seen, the SFHs exhibit similar behavior and there is only a shift towards recent times with increasing distance modulus. The Galactic extinctions for And IX are estimated $A_i = 0.127 \text{ mag}$ ($E(B-V) = 0.075$ (McConnachie 2012)) and $A_i = 0.129 \text{ mag}$ ($E(B-V) = 0.076$ (Conn et al. 2012)) from the Schlafly & Finkbeiner (2011). In Fig. 22, we compare the SFH of the galaxy, assuming the average of the reported Galactic extinctions ($A_i =$

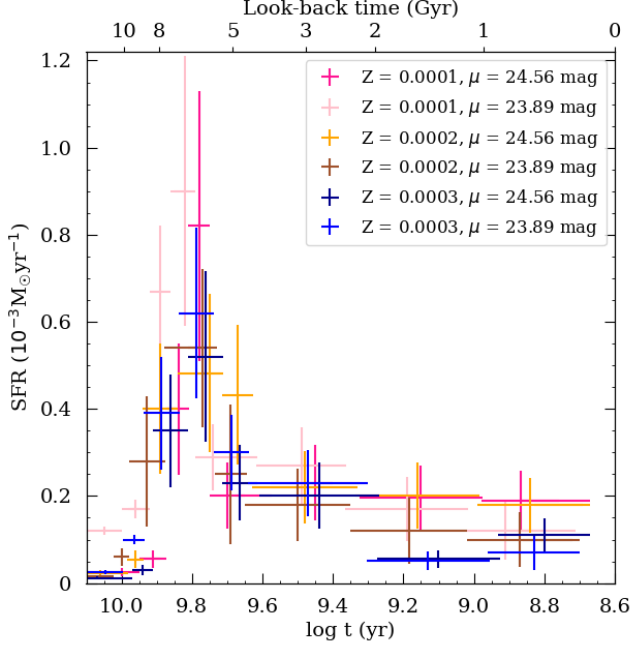


Figure 21. SFHs of And IX for three metallicities of $Z = 0.0001$, $Z = 0.0002$, and $Z = 0.0003$ within two half-light radii ($\sim 0.022 \text{ deg}^2$) in distance modulus of $23.89^{+0.31}_{-0.08} \text{ mag}$ (Weisz et al. 2019a) and $24.56^{+0.05}_{-0.15} \text{ mag}$.

0.128 mag), with the SFH of And IX, which does not account for Galactic extinction ($A_i = 0 \text{ mag}$). There is no significant difference in results, but the SFH is shifted to earlier epochs when the Galactic extinction is ignored.

We estimate the total stellar mass of And IX in the lowest distance modulus ($23.89^{+0.31}_{-0.08} \text{ mag}$ (Weisz et al. 2019a)) $\sim 3.50 \pm 0.50 \times 10^5 M_{\odot}$ with $A_i = 0.128 \text{ mag}$, and $\sim 3.10 \pm 0.30 \times 10^5 M_{\odot}$ with $A_i = 0 \text{ mag}$, at $Z = 0.0001$. In metallicity of $Z = 0.0002$, the total stellar mass is $\sim 2.70 \pm 0.40 \times 10^5 M_{\odot}$ with $A_i = 0.128 \text{ mag}$ and $\sim 2.60 \pm 0.10 \times 10^5 M_{\odot}$ with $A_i = 0$. The total stellar mass of And IX at $Z = 0.0003$ is $\sim 2.50 \pm 0.40 \times 10^5 M_{\odot}$ and $\sim 2.46 \pm 0.20 \times 10^5 M_{\odot}$ considering $A_i = 0.128 \text{ mag}$ and $A_i = 0 \text{ mag}$, respectively.

As a function of look-back time and redshift, Fig. 23 shows the cumulative star formation (colors based on Fig. 20). The best exponential fit for our star formation model was obtained with the τ -model with $\tau = 5$. The equation describes SFH with declining e-folding time " τ ", which is initiated at " t_i " with amplitude " A " (Simha et al. 2014);

$$SFR(t) \propto A e^{-(t-t_i)/\tau}. \quad (6)$$

According to Fig. 23, the horizontal dashed line labeled 90% M_{tot} indicates the time it took to assemble 90% of the stellar mass (known quenching time). In addition, Fig. 23 shows the epoch by which 50% of the stellar mass had been formed with a horizontal dashed line indicating 50% M_{tot} .

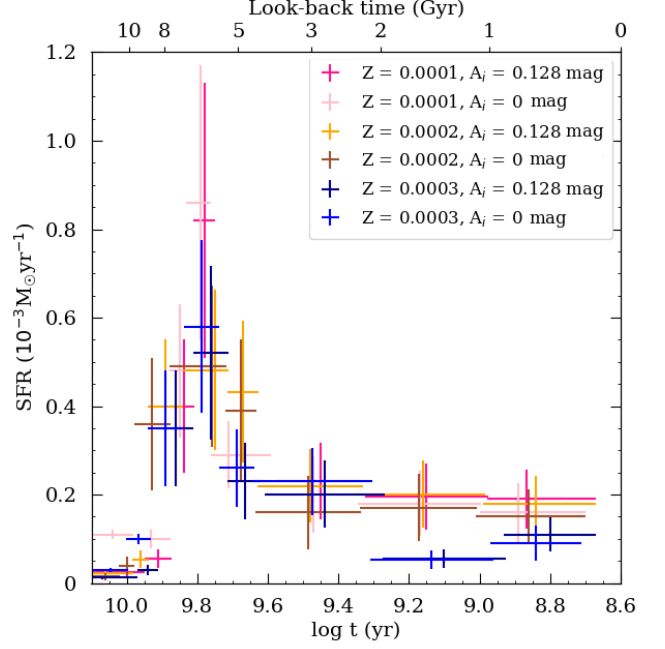


Figure 22. SFHs of And IX for three metallicities of $Z = 0.0001$, $Z = 0.0002$, and $Z = 0.0003$ within two half-light radii ($\sim 0.022 \text{ deg}^2$) with applying the Galactic extinction in filter i ($A_i = 0.128 \text{ mag}$) and without considering the extinction ($A_i = 0 \text{ mag}$).

Table 4 summarizes the aggregation time for half (t_{50}) and 90% (t_{90}) of the total stellar mass in different metallicities of And IX. The first line in t_{50} and t_{90} of Table 4 is based on SFHs in Fig. 20 and distance modulus of $24.56^{+0.05}_{-0.15}$, the second line is based on the SFH with distance modulus $23.89^{+0.31}_{-0.08} \text{ mag}$ in Fig. 21. According to Table 4, the aggregation time for 50% and 90% of the total stellar mass move to the recent times in three metallicities by increasing the distance modulus. Additionally, increasing metallicity has a similar effect on t_{50} and t_{90} at the same distance modulus. Our results are consistent with Weisz et al. (2019b), who estimated the quenching time as $5.1^{+1.8}_{-2.0} \text{ Gyr}$ ago and the aggregation of half of the total stellar mass as $7.2^{+2.5}_{-0.3} \text{ Gyr}$ ago.

6.3. Radial star formation history

SFHs in different radial regions within a galaxy may reveal important information regarding the galaxy's formation history. For this, we divided the area of And IX into different radius bins with an equal number of stars to derive the radial gradient of SFH. In Fig. 24, the density of the SFR is plotted as a function of logarithmic time in four circular regions for metallicity $Z = 0.0001$. Due to the four annuli that make up And IX, each region may have a different population of stars. The ratio of the SFR for $t > 3.16 \text{ Gyr ago}$ ($\log(t) > 9.5$) to that for $t < 3.16 \text{ Gyr ago}$ ($\log(t) < 9.5$) in the innermost region is $0.990^{+0.005}_{-0.010}$, while in the second region ($\sim 0.35 - 0.61 \text{ kpc}$) it is $1.82^{+0.07}_{-0.04}$. The fraction reaches $1.45^{+0.03}_{-0.06}$ in the third

Table 4. Time to aggregation for half of the total stellar mass (t_{50}) and 90% of the total stellar mass (t_{90}) in different metallicities.

	$\mu(mag)$	$Z = 0.0001$	$Z = 0.0002$	$Z = 0.0003$
t_{50} (Gyr)	$24.56^{+0.05}_{-0.15}$ ^a	$7.02^{+0.39}_{-0.56}$	$6.15^{+0.77}_{-1.02}$	$6.10^{+0.36}_{-0.97}$
	$23.89^{+0.31}_{-0.08}$ ^b	$8.00^{+0.10}_{-1.30}$	$7.20^{+0.80}_{-0.70}$	$7.10^{+0.30}_{-1.40}$
t_{90} (Gyr)	$24.56^{+0.05}_{-0.15}$	$3.65^{+0.13}_{-1.52}$	$3.29^{+0.97}_{-1.16}$	$3.07^{+1.00}_{-1.39}$
	$23.89^{+0.31}_{-0.08}$	$3.95^{+2.00}_{-0.50}$	$3.40^{+0.40}_{-0.60}$	$3.10^{+0.30}_{-0.40}$

^aEstimates based on the distance modulus calculated in this paper

^bEstimates based on the distance modulus calculated in Weisz et al. (2019a)

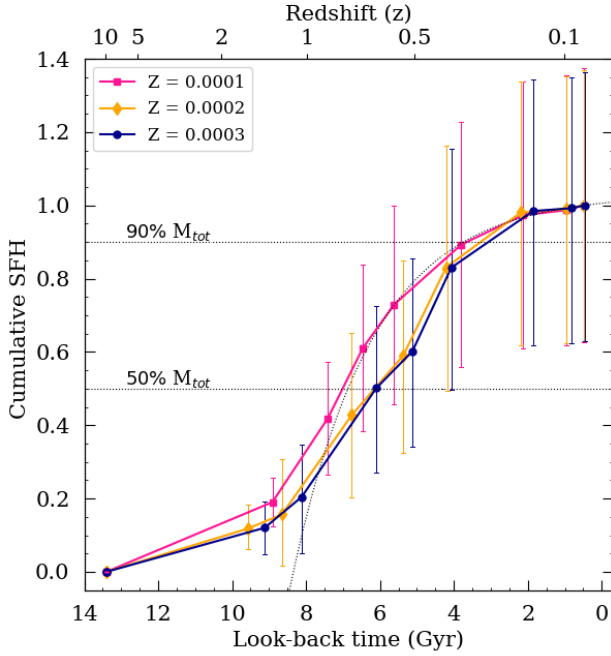


Figure 23. Cumulative SFH as a function of look-back time and redshift within two half-light radii of And IX for three different adopted metallicities. Each bin is accompanied by a vertical error bar showing the statistical error of the SFR. The pink curve is also fitted by a τ -model exponential function (the dotted black curve). Statistical errors in SFRs indicate the cumulative SFH errors for metallicities of $Z = 0.0001$ (pink error bars), $Z = 0.0002$ (orange error bars), and $Z = 0.0003$ (blue error bars).

region and $3.48^{+0.91}_{-0.40}$ in the outermost region. When moving toward central regions, this ratio decreases, suggesting that younger populations tend to be concentrated there. As a result, star formation began in the outer part and gradually spread inward. In these regions, 20% of the total mass per unit area is formed at the outermost radius, 23% at the middle regions, and the rest at the innermost radius. Therefore, the total stellar mass per unit area is more concentrated in the innermost region.

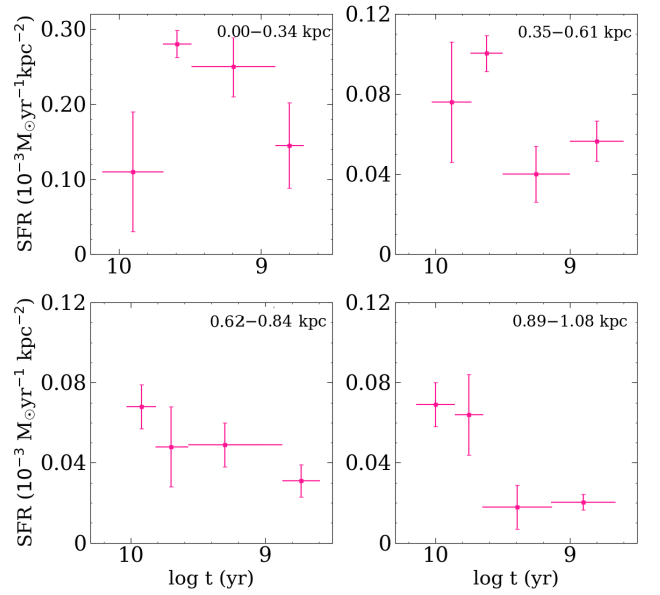


Figure 24. SFR of And IX per unit area within four regions at galactocentric radii for a constant metallicity of $Z = 0.0001$.

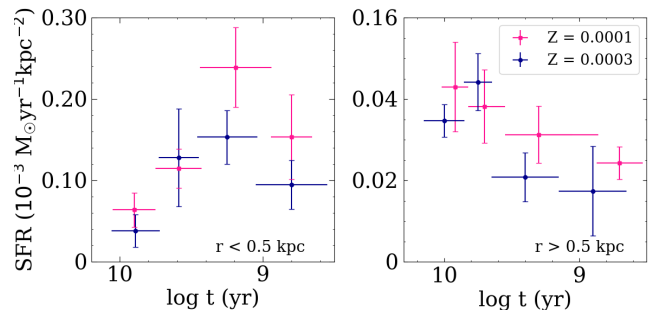


Figure 25. SFR of And IX per unit area with equal numbers of LPV candidates within two regions at galactocentric radii for metallicities of $Z = 0.0001$ (pink) and $Z = 0.0003$ (blue).

In Fig. 25, we divided our sample into two regions ($r < 0.5$ and $r > 0.5$ kpc) to examine the radial gradient of SFH for metallicities $Z = 0.0001$ (in pink) and $Z = 0.0003$ (in blue). The star formation pattern suggests the highest SFRs in central regions at later times, which is the opposite of the outer regions. In support of this, the fractions of $0.720^{+0.003}_{-0.002}$ in $r < 0.5$, and $2.13^{+0.77}_{-0.29}$ in $r > 0.5$ are obtained by estimating the ratio of the older population at $Z = 0.0001$ compared to the younger population at $Z = 0.0003$. When $r > 0.5$ kpc (estimated ratio greater than unity), older populations form earlier than when $r < 0.5$ kpc (estimated ratio less than unity). Obviously, this supports the outside-in formation scenario of And IX based on the different age gradients of the population in the inner and outer parts of the galaxy (Hidalgo et al. 2008; Hidalgo et al. 2013; Benítez-Llambay et al. 2016). The dynamical effect could be another scenario for the distribution of stars in And IX, where stars migrate outwards after forming in more central regions. This is not unexpected as star formation only occurs if gas cools and falls deeply into the gravitational potential well of a small halo such as And IX; this is a highly non-equilibrium state, and internal dynamics would gradually cause the stars to fill the gravitational potential well (i.e., migrate outward); tidal stress would exacerbate that.

6.4. Quenching mechanisms in And IX

Several mechanisms lead to the quenching of a dwarf galaxy. Depletion of cold gas in the re-ionization era is supposed to affect the shutting-down of star formation in ultra-faint dwarfs ($M_V > -6$ mag) and low-mass galaxies ($M < 10^5 M_\odot$) (Gnedin 2014; Xu et al. 2016; Wheeler et al. 2019; Applebaum et al. 2021). At $z = 10$, low-mass galaxies are expected to be quenched by cosmic re-ionization, while for more massive galaxies, environmental processes have a more significant effect on the cessation of star formation at $z = 6$ (Wetzel et al. 2015). It can be ruled out with greater certainty that the epoch of re-ionization will not affect And IX's quiescent since the SFRs are shut-down by $z = 6$. Environmental effects, such as ram-pressure stripping, tidal effects, and dwarf-galaxy interactions, may quench dwarfs with stellar masses of $10^5 - 10^7 M_\odot$. In particular, ram-pressure stripping is a noticeable mechanism to stop star formation in galaxies with $M < 10^7 M_\odot$ (Simpson et al. 2018).

Another factor in the shutting-down of star formation of a satellite can be the fall in the virial radius of its host galaxy. For the Milky Way dwarf satellite galaxies, the infall time can be calculated using positions, line-of-sight velocities, and proper motions (if measured) (Rocha et al. 2012). Since these data are not available for satellites of Andromeda, cosmological simulation is used to estimate the infall time. In a study by Wetzel et al. (2015), all Milky Way and Andromeda satellites with $M < 10^8 M_\odot$ have been quenched after falling into their

host galaxy's virial radius of fewer than 2 Gyr, and quenching is more rapid at lower stellar masses. This study estimated infall time using N-body simulations. Furthermore, D'Souza & Bell (2021) proposed a correlation between quenching time and the time when satellites enter the virial halo of their hosts (accretion time). In M31, massive accretion occurred around 5.5 Gyr ago, around the time most M31 satellites quenched and also our estimate. Using 20 satellites of M31, Weisz et al. (2019b) determined a look-back time of 3 – 6 Gyr for the assembly of 90% of stellar mass and 6 – 9 Gyr for the assembly of 50% of stellar mass. Our study also confirms these results. For metallicities of $Z = 0.0004$ and $Z = 0.0007$, Saremi et al. (2021) estimated the quenching time of And I about 4 Gyr ago. Similarly, And VII, another satellite of M31, was quenched 5 Gyr ago at $Z = 0.0007$ and 5.7 Gyr ago at $Z = 0.0004$ (Navabi et al. 2021). It is also consistent with the quenching time reported in Weisz et al. (2019b).

Environmental processes play an essential role in quenching And IX, a satellite with a stellar mass of $M \leq 10^8 M_\odot$. These processes include tidal effects and the depletion of cold gas through M31 (due to proximity). Internal processes also quench star formation, such as galactic winds, supernovae, and stellar feedback, specifically in low-mass dwarfs (Ledinauskas & Zubovas 2020).

7. PROBING OF DUST IN AND IX

7.1. C-rich and O-rich circumstellar envelopes

The carbon abundance in the atmosphere of AGB stars increases after the third dredge-up process, despite the abundance of oxygen before it. Based on carbon and oxygen abundances in the atmosphere, AGBs are generally classified as carbon-rich ($C/O > 1$) or oxygen-rich ($C/O < 1$) (Ren et al. 2022). As metal-poor environments have less oxygen, carbon stars form more easily since less carbon must be dredged-up to achieve $C/O > 1$ (Leisenring et al. 2008; Ren et al. 2022). AGB star models estimate different thresholds for the third dredge-up, some of which are summarised below. In Magellanic Clouds (MCs), the mass range for C-rich stars is between $1.3 - 4 M_\odot$ (van Loon et al. 2005b); Girardi & Marigo (2007) estimate the mass ranges of C- and M-type stars using $1.5 - 2.8 M_\odot$ for C-rich stars in MCs clusters. According to McDonald et al. (2012), the condition of $C/O > 1$ was first achieved in stars around $1 M_\odot$ in the Sgr dSph galaxy with metallicity $Z \sim 4 \times 10^{-3}$. In LMC, Goldman et al. (2017) estimations of $M \leq 1.5 M_\odot$ and $M \geq 4 M_\odot$ for O-rich stars are based on 1612 MHz circumstellar OH maser emissions from AGB stars and RSGs.

Given the low oxygen abundance in And IX, a range of $1.5 - 4 M_\odot$ is adopted for the carbon stars (Saremi et al. 2021). In our survey, no LPVs were found in the mass range of $1 - 1.5 M_\odot$, thus substantial differences are not seen in the number of C- and O-rich LPVs based on these assumptions.

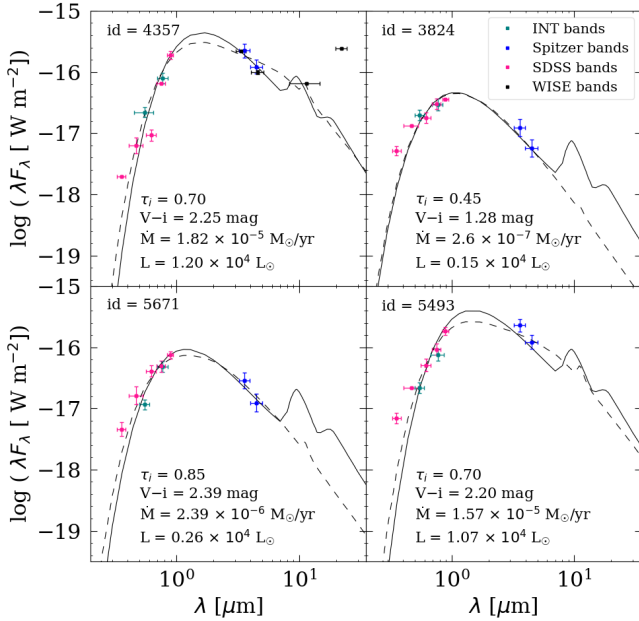


Figure 26. Example SEDs of LPVs with the best fit for the C- and O-rich type of AGBs (dashed and solid black lines). Fluxes are modelled by `DUSTY` as a function of wavelength. Fluxes observed in different bands with the INT (i and V), *Spitzer* (3.6 and 4.5 μm), SDSS (u , g , r , i , and z), and WISE (W_1 , W_2 , W_3 , and W_4) are shown by green, blue, pink, and black squares, respectively. Vertical and horizontal error bars show photometric uncertainty in the magnitude and the difference between the λ_{max} and λ_{min} around each filter’s central wavelength, respectively.

As a result, the SFRs are almost the same regardless of the precise choice of the lower end of the C-rich star mass range. The chemical type of stars is determined by their masses, as described in Section 6.

7.2. SED modelling through `DUSTY`

In this paper, we modelled the SEDs of variables through the `DUSTY` code, which was written by Ivezic & Elitzur (1997). Modelling the SED requires input data such as stellar temperature, external radiation characteristics, dust properties (e.g., temperature, chemical compositions, grain size distribution), optical depth, and envelope density distribution. We put the star’s and dust’s temperatures at the inner edge of circumstellar envelope 3000 – 3500 K and 500 – 1200 K, respectively (Gail & Sedlmayr 1999; Höfner & Olofsson 2018). The C-rich type is made through the mixture of 85% amorphous carbon (Hanner 1988) and 15% silicon carbide (Pégourié 1988), while the O-rich type is made through the use of astronomical silicates (Draine & Lee 1984). In solving hydrodynamic equations for AGB stars, `DUSTY` assumes radiatively driven wind. When solving the equation, the default parameters

(gas-to-dust mass ratio $\psi_{\odot} = 200$, $L = 10^4 L_{\odot}$, and $\rho_{\text{dust}} = 3 \text{ g cm}^{-3}$) are adopted. In this case, ψ is scaled by the relation $\psi = \psi_{\odot} 10^{-[Fe/H]}$ assuming the reverse metallicity relation with the gas-to-dust mass ratio (van Loon et al. 2005b). Based on trial and error, the optical depth is estimated by comparing the simulated SED to the observed SED. As a result of the scaling relations, the mass-loss rates of LPVs are determined using the following equation (Nenkova et al. 1999):

$$\dot{M} = \dot{M}_{\text{DUSTY}} \left(\frac{L}{10^4} \right)^{3/4} \left(\frac{\psi}{\psi_{\odot}} \right)^{1/2} \quad (7)$$

Examples of SEDs obtained with INT (i and V), *Spitzer* (3.6 and 4.5 μm), SDSS (u , g , r , i , and z), and WISE (W_1 , W_2 , W_3 , and W_4) are shown in Fig. 26. The best fit curves are constructed for two types of dust (solid and dashed black curves for O- and C-rich LPVs, respectively). Besides the best fit for the preferred dust species, we also show the best fit for the alternative dust species. Table 6 in the Appendix describes the physical properties of LPVs, which contains information such as star id, coordinates, magnitude (V) and error of magnitude (δV) in Harris V filter, magnitude (i) and error of magnitude (δi) in Sloan i' filter, amplitude in Sloan i' filter (amplitude $_i$), birth mass (M_{Birth}), optical depth in Sloan i' (τ_i), mass-loss rate (\dot{M}), luminosity (L), and chemical type of LPVs.

Fig. 27 shows mass-loss rates for C-rich (red squares) and O-rich (green triangles) LPVs as a function of luminosity. In order to assess the effect of chemical types of dust on optical depth and mass-loss ratio, carbon stars were assumed to have oxygen dust (open red squares). Changing optical depth under the effect of dust species alters the mass-loss ratio and luminosity of this sample. Based on van Loon et al. (1999)’s paper, this figure shows the maximum and classical limit of mass-loss rates. The maximum mass-loss rate ridgeline is an extreme envelope of rates that were measured once in the past (van Loon et al. 1999), and given the uncertainties in those data and modelling assumptions, the actual limit may be somewhat lower; hence we added a question mark to it. The black squares in this figure indicate Boyer et al. (2015b)’s x-AGBs with specific ids. We have used SED modeling to estimate all four x-AGBs’ mass-loss (and luminosity). As shown in this figure, the two x-AGBs are mutual with the INT and *Spitzer* surveys, and two other Boyer et al. (2015b)’s variables were identified in the INT survey as non-variables. This plot shows that LPVs in And IX have mass-loss rates of $1.7 \times 10^{-7} \leq \dot{M} \leq 1.9 \times 10^{-5} M_{\odot} \text{ yr}^{-1}$ and luminosity of $8.0 \times 10^2 \leq L \leq 1.2 \times 10^4 L_{\odot}$. It is estimated that the mass-loss rate of the two mutual x-AGBs is about 3.6% of the total mass return rate, while if four x-AGBs were identified, this rate would be 5.7%. The maximum mass-loss rate of our LPVs ($\sim 10^{-5} M_{\odot} \text{ yr}^{-1}$) is around 2 dex less than the upper limit of maximum mass-loss rates of AGBs in the LMC

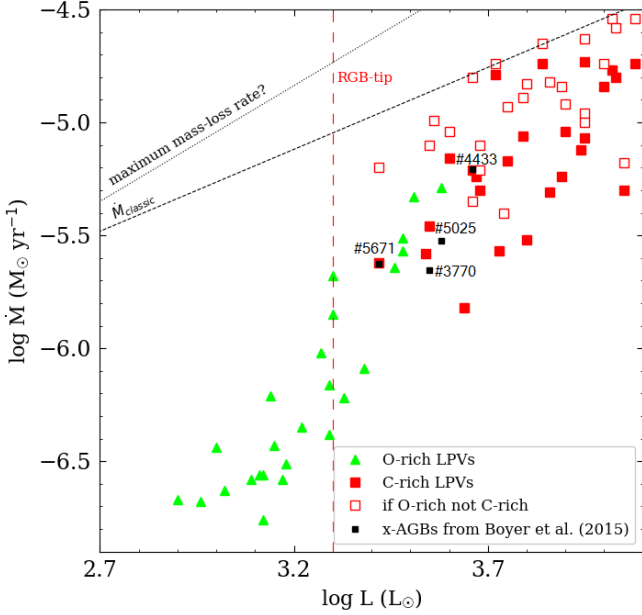


Figure 27. Mass-loss rate as a function of luminosity for C-rich (red squares) and O-rich (green triangles) LPVs within two half-light radii of And IX. The open red squares would show the results if the carbon stars were assumed instead to be O-rich. A dotted line represents the classical single scattering mass-loss limits $\dot{M}_{\text{classic}} \propto L^{0.75}$, and the mass-loss limits when multiple scattering of photons becomes important (maximum mass-loss rate?) is represented by the dashed line (van Loon et al. 1999). The tip luminosity of the RGB is marked with the red vertical dashed line. Four x-AGBs of Boyer et al. (2015b) are highlighted with their ids, two of which are mutual in *Spitzer* and INT surveys.

($10^{-7} - 10^{-3} M_{\odot} \text{ yr}^{-1}$) (van Loon et al. 1999). In more metal-poor environments, such as in WLM galaxy with metallicity of $[\text{Fe}/\text{H}] = 1.13$, the mass-loss rate of AGBs is calculated to be $10^{-10} - 10^{-4} M_{\odot} \text{ yr}^{-1}$ for O-rich AGBs and $10^{-10} - 10^{-5} M_{\odot} \text{ yr}^{-1}$ for C-rich ones (Jackson et al. 2007).

Mass-loss rate increases during stellar evolution along the AGB phase synchronously with luminosity (and hence birth mass) (Höfner & Olofsson 2018). Fig. 27 illustrates the same point, as most luminous stars generally reach higher mass-loss rates. If LPVs with masses greater than $1.5 M_{\odot}$ are assumed to be O-rich, the mass-loss rate would be higher. Due to the lower opacity of silicates compared to amorphous carbon grains, fitting carbon stars with silicates usually results in higher mass-loss rates. In this diagram, the carbon star with luminosity $0.89 \times 10^4 L_{\odot}$ has the most mass-loss $1.87 \times 10^{-5} M_{\odot} \text{ yr}^{-1}$. With silicon dust, the mass-loss of this star increases by 25%. As illustrated in Fig. 27, mass-loss variance is evident around the RGB-tip in a given luminosity (birth mass), indicating star evolution throughout the galaxy (Javadi et al. 2013). When a star climbs the AGB, its mass-

loss increases gradually with luminosity, allowing different mass-losses to be observed at the same luminosity. Carbon stars tend to have higher luminosities and mass-losses because of their higher mass; however, some carbon stars have lower luminosities ($\log L < 3.6 L_{\odot}$ in Fig. 27) and mass-losses than oxygen stars. These carbon stars may be in the inter-thermal pulse luminosity dip and experience lower luminosity and mass-loss rate, whereas, after thermal pulses, they experience higher luminosity and mass-loss rate (Vassiliadis & Wood 1993; Mattsson et al. 2007). On the other hand, the metallicity gradient in galaxies can also lead to overlaps between carbon and oxygen stars, which seem unlikely here. Even if there is a metallicity gradient in this galaxy, since we did not detect any stars in the range of 1 to $1.5 M_{\odot}$, changing this limit due to metallicity does not affect our results. The limit at which oxygen stars turn into carbon stars is affected by metallicity. Oxygen stars with higher mass-loss and luminosity than carbon stars have spent more time evolving in the AGB phase, the luminosity of these carbon stars can also increase with further evolution in this phase (Marigo et al. 2008).

The results of the total mass return rate and the ratio of the total mass return to the total stellar mass at three different metallicities are summarized in Table 5. Moreover, we estimated the ratio of the total mass return rate to the total stellar mass of LPVs. This ratio is a measure of the duration of the dominant mass-loss phase or rather the inverse of it. In fact, it sets an upper limit to the duration, as the stars do not completely vanish but leave remnants (white dwarfs, neutron stars, or black holes). With $Z = 0.0001$, the timescale is 3.0×10^5 yr, which is a few times shorter than the radial pulsation-phase timescale of $\sim 10^6$ yr as predicted by the models (Saremi et al. 2021). Based on this, the more extreme phase of the LPV and heavy mass-loss seems to last for a shorter period of time than the whole TP-AGB lifetime. Also, we estimated the specific mass-loss rate as the total mass return by the total stellar mass in each metallicity. It is estimated that the mass-loss of LPVs in about a billion years could enrich the ISM and revive star formation in the galaxy. Despite this, the mass of the ISM may be impacted by the interaction with the M31 galaxy. We can refer to Buck et al. (2019)’s simulation for more information on the possibility of mass-loss in satellites in LG, such as And IX, via stripping. Based on this simulation, it was found that satellite galaxies have a lower present-day stellar mass ($z = 0$) than the maximum total mass they have ever reached during their evolution. Accordingly, satellite galaxies with present-day stellar masses of order $\sim 10^6 M_{\odot}$ had a maximum stellar mass of order $\sim 10^9 M_{\odot}$ (Buck et al. 2019).

The total stellar mass and the total mass return rate in And IX are decreased with increasing metallicity. So the specific mass-loss rate follows this pattern. C-rich and O-rich LPVs have total mass-loss rates of $2.1 \times 10^{-4} M_{\odot} \text{ yr}^{-1}$ and

Table 5. Estimations of the mass-loss ratios of And IX LPVs in different metallicities.

Metallicity	\dot{M}^a ($10^{-4} M_{\odot} \text{ yr}^{-1}$)	\dot{M} ($10^{-4} M_{\odot} \text{ yr}^{-1}$) (if all O-rich)	\dot{M}/M_{LPV}^b (10^{-6} yr^{-1})	Specific mass-loss rate (10^{-10} yr^{-1})
$Z = 0.0001$	2.4	3.7	3.0	8.0
$Z = 0.0002$	1.5	2.4	2.0	6.0
$Z = 0.0003$	1.0	1.7	1.0	4.0

^aTotal mass return rate

^bTotal stellar mass of LPVs

$2.9 \times 10^{-5} M_{\odot} \text{ yr}^{-1}$ at $Z = 0.0001$, respectively. As carbon stars account for about 80% of the total mass return rate in three metallicities, most of the dust that enters the ISM by LPVs is carbon dust.

8. SUMMARY

From June 21, 2015, to October 6, 2017, nine observations were undertaken to study the properties of And IX, the dwarf spheroidal satellite of the M31. Observations were conducted using the 2.5-m wide-field camera (WFC) of the INT with the Sloan i' and Harris V filters. We detected 54 AGB candidates within two half-light radii (~ 5 arcmin) of And IX by employing DAOPHOT/ALLSTAR software (Stetson 1987, 1990, 1996). About 50 of them are LPVs with amplitude $_i > 0.2$ mag. We calculated the SFRs as a galaxy evolution tracer in two half-light radii for metallicities of $Z = 0.0001, 0.0002, 0.0003$. Due to the temperature and radius variations, LPVs experience significant mass-loss in the form of a stellar wind. We measure mass-loss rates using multi-wavelength data from INT, *Spitzer*, SDSS, and WISE. Our primary conclusions are as follows:

- The maximum rate of star formation $\sim 8.2 \pm 3.1 \times 10^{-4} M_{\odot} \text{ yr}^{-1}$ occurred 6 Gyr ago at $Z = 0.0001$. Compared to the peak of SFR in the more metal-rich estimation ($\sim 5.2 \pm 2.0 \times 10^{-4} M_{\odot} \text{ yr}^{-1}$ at 5.7 Gyr ago), the peak of SFR in the more metal-poor estimation is 57% higher.
- The total stellar mass is estimated $\sim 3.0 \times 10^5 M_{\odot}$ ($Z = 0.0001$), which decreased up to $2.3 \times 10^5 M_{\odot}$ by increasing metallicity to $Z = 0.0003$. Furthermore, based on And IX's cumulative SFH, 90% of its total stellar mass was formed until $\sim 3.65^{+0.13}_{-1.52}$ Gyr ago at $Z = 0.0001$, indicating that this galaxy had an extended SFH. Furthermore, half of the mass of the And IX was formed about $7.02^{+0.39}_{-0.56}$ Gyr ago in more metal-poor estimation. Consequently, our results imply that this dSph satellite was quenched late, possibly due to late infall.
- And IX shows a late epoch of star formation, peaking around 630 Myr ago, but the SFR is low $1.1 \pm 0.4 \times 10^{-4}$

$M_{\odot} \text{ yr}^{-1}$. In this quenched galaxy, dusty stellar winds at earlier times may have contributed to this late epoch of star formation.

- According to the different age gradients of the population in the inner and outer parts of the galaxy, the outside-in star formation scenario could be a galaxy evolution scenario. Furthermore, the separation of population ages might result from stars migrating outward after forming in more central regions.
- We estimated the mass-loss rate of LPVs ($10^{-7} - 10^{-5} M_{\odot} \text{ yr}^{-1}$) employing DUSTY code (Ivezic & Elitzur 1997). We have shown a correlation between mass-loss rates and luminosity for AGB stars. However, there is also an evolution term for stars of a given mass that should be considered. In addition, the carbon stars contribute much to the replenishment of the ISM with a timescale of $\sim 3.0 \times 10^5$ yr, a few times shorter than the TP-AGB duration. Also, we calculated the total mass returned rate to the ISM by LPVs $\sim 1.0 - 2.4 \times 10^{-4} M_{\odot} \text{ yr}^{-1}$ depending on the adopted metallicity. The mass-loss of LPVs could enrich the ISM in about a billion years if external or internal processes do not remove the gas.

9. ACKNOWLEDGEMENTS

The observing time for this survey was provided by the Iranian National Observatory (INO) and the UK-PATT allocation of time to programs I/2016B/09 and I/2017B/04 (PI: J. van Loon). We thank the INO and the School of Astronomy (IPM) for the financial support of this project. We thank the referee for their comments which helped enhance the analysis. HA is grateful to Peter Stetson for sharing his photometry routines. We thank Alireza Molaeinezhad, Arash Danesh, Mojtaba Raouf, Ghassem Gozaliasl, James Bamber, Philip Short, Lucia Suárez-Andrés, and Rosa Clavero for their help with the observations.

REFERENCES

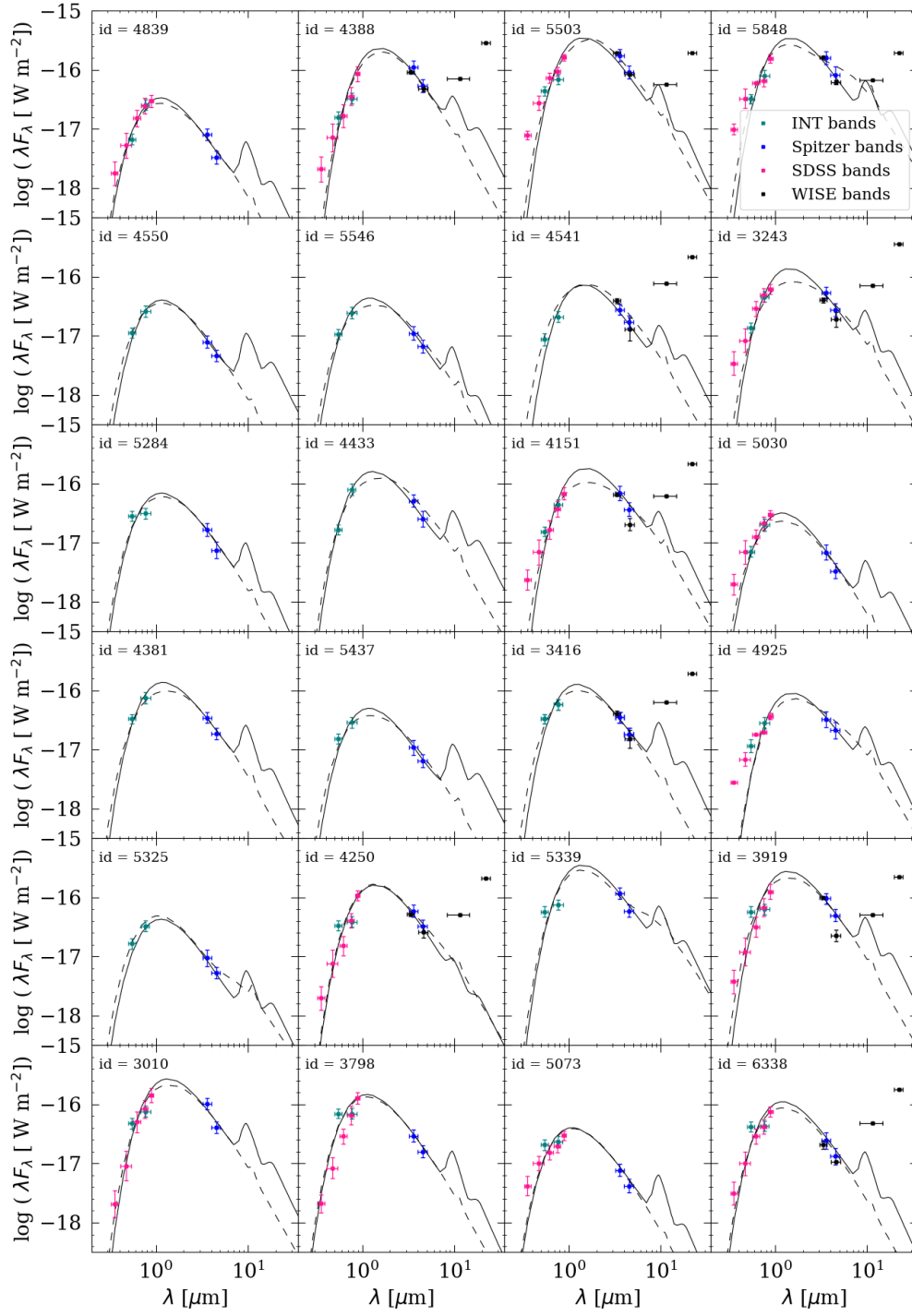
- Applebaum E., Brooks A. M., Christensen C. R., Munshi F., Quinn T. R., Shen S., Tremmel M., 2021, *ApJ*, **906**, 96
- Battinelli P., Demers S., 2013, Publications de l'Observatoire Astronomique de Beograd, **92**, 117
- Benítez-Llambay A., Navarro J. F., Abadi M. G., Gottlöber S., Yepes G., Hoffman Y., Steinmetz M., 2016, *MNRAS*, **456**, 1185
- Boyer M. L., Skillman E. D., van Loon J. T., Gehrz R. D., Woodward C. E., 2009, *ApJ*, **697**, 1993
- Boyer M. L., et al., 2012, *ApJ*, **748**, 40
- Boyer M. L., et al., 2015a, *ApJS*, **216**, 10
- Boyer M. L., et al., 2015b, *ApJ*, **800**, 51
- Boylan-Kolchin M., Bullock J. S., Kaplinghat M., 2011, *MNRAS*, **415**, L40
- Boylan-Kolchin M., Bullock J. S., Kaplinghat M., 2012, *MNRAS*, **422**, 1203
- Bressan A., Marigo P., Girardi L., Salasnich B., Dal Cero C., Rubele S., Nanni A., 2012, *MNRAS*, **427**, 127
- Buck T., Macciò A. V., Dutton A. A., Obreja A., Frings J., 2019, *MNRAS*, **483**, 1314
- Cignoni M., Tosi M., 2010, *Advances in Astronomy*, **2010**, 158568
- Collins M. L. M., et al., 2010, *MNRAS*, **407**, 2411
- Conn A. R., et al., 2012, *ApJ*, **758**, 11
- Cutri R. M., et al., 2021, VizieR Online Data Catalog, p. II/328
- D'Souza R., Bell E. F., 2021, *MNRAS*, **504**, 5270
- Del Popolo A., Le Delliou M., 2017, *Galaxies*, **5**, 17
- Draine B. T., Lee H. M., 1984, *ApJ*, **285**, 89
- Fillingham S. P., et al., 2019, arXiv e-prints, p. arXiv:1906.04180
- Gaia Collaboration et al., 2021, *A&A*, **649**, A1
- Gail H. P., Sedlmayr E., 1999, *A&A*, **347**, 594
- Girardi L., Marigo P., 2007, *A&A*, **462**, 237
- Girardi L., Groenewegen M. A. T., Hatziminaoglou E., da Costa L., 2005, *A&A*, **436**, 895
- Gnedin N. Y., 2014, *ApJ*, **793**, 29
- Goldman S. R., et al., 2017, *MNRAS*, **465**, 403
- Goldman S. R., et al., 2019, *ApJ*, **877**, 49
- Hamedani Golshan R., Javadi A., van Loon J. T., Khosroshahi H., Saremi E., 2017, *MNRAS*, **466**, 1764
- Hanner M. S., 1988, Infrared Observations of Comets Halley and Wilson and Properties of the Grains
- Harbeck D., Gallagher J. S., Grebel E. K., Koch A., Zucker D. B., 2005, *ApJ*, **623**, 159
- Hashemi S. A., Javadi A., van Loon J. T., 2019, *MNRAS*, **483**, 4751
- Hidalgo S. L., Aparicio A., Gallart C., 2008, *The Astronomical Journal*, **136**, 2332
- Hidalgo S. L., et al., 2013, *ApJ*, **778**, 103
- Höfner S., Olofsson H., 2018, *A&A Rv*, **26**, 1
- Ivezic Z., Elitzur M., 1997, *MNRAS*, **287**, 799
- Jackson D. C., Skillman E. D., Gehrz R. D., Polomski E., Woodward C. E., 2007, *ApJ*, **656**, 818
- Javadi A., van Loon J. T., Mirtorabi M. T., 2011a, *MNRAS*, **411**, 263
- Javadi A., van Loon J. T., Mirtorabi M. T., 2011b, *MNRAS*, **414**, 3394
- Javadi A., van Loon J. T., Khosroshahi H., Mirtorabi M. T., 2013, *MNRAS*, **432**, 2824
- Javadi A., Saberi M., van Loon J. T., Khosroshahi H., Golabatooni N., Mirtorabi M. T., 2015, *MNRAS*, **447**, 3973
- Javadi A., van Loon J. T., Khosroshahi H. G., Tabatabaei F., Hamedani Golshan R., Rashidi M., 2017, *MNRAS*, **464**, 2103
- Jordi K., Grebel E. K., Ammon K., 2006, *A&A*, **460**, 339
- Kirby E. N., Cohen J. G., Guhathakurta P., Cheng L., Bullock J. S., Gallazzi A., 2013, *ApJ*, **779**, 102
- Klypin A., Kravtsov A. V., Valenzuela O., Prada F., 1999, *ApJ*, **522**, 82
- Kroupa P., 2001, *MNRAS*, **322**, 231
- Ledinauskas E., Zubovas K., 2020, *MNRAS*, **493**, 638
- Lee M. G., Freedman W. L., Madore B. F., 1993, *ApJ*, **417**, 553
- Leisenring J. M., Kemper F., Sloan G. C., 2008, *ApJ*, **681**, 1557
- Lupton R. H., 2005, MS Windows NT Kernel Description, <https://www.sdss3.org/dr8/algorithms/sdssUBVRITransform.php>
- Marigo P., Girardi L., Bressan A., Groenewegen M. A. T., Silva L., Granato G. L., 2008, *A&A*, **482**, 883
- Marigo P., et al., 2017, *ApJ*, **835**, 77
- Mattsson L., Höfner S., Herwig F., 2007, *Astronomy & Astrophysics*, **470**, 339
- McConnachie A. W., 2012, *AJ*, **144**, 4
- McConnachie A. W., Irwin M. J., Ferguson A. M. N., Ibata R. A., Lewis G. F., Tanvir N., 2004, *MNRAS*, **350**, 243
- McConnachie A. W., Irwin M. J., Ferguson A. M. N., Ibata R. A., Lewis G. F., Tanvir N., 2005, *MNRAS*, **356**, 979
- McDonald I., Trabucchi M., 2019, *MNRAS*, **484**, 4678
- McDonald I., Zijlstra A. A., 2016, *ApJL*, **823**, L38
- McDonald I., White J. R., Zijlstra A. A., Guzman Ramirez L., Szyszka C., van Loon J. T., Lagadec E., Jones O. C., 2012, *MNRAS*, **427**, 2647
- Müller O., et al., 2021, *A&A*, **645**, A92
- Navabi M., et al., 2021, *ApJ*, **910**, 127
- Navarro J. F., 2018, *Proceedings of the International Astronomical Union*, **14**, 455–463
- Nenkova M., Ivezic Z., Elitzur M., 1999, in Sprague A., Lynch D. K., Sitko M., eds, LPI Contributions Vol. 969, Thermal Emission Spectroscopy and Analysis of Dust, Disks, and Regoliths. p. 20
- Parto T., et al., 2023, *ApJ*, **942**, 33
- Pégourié B., 1988, *Astronomy and Astrophysics*, **194**, 335
- Planck Collaboration et al., 2014, *A&A*, **571**, A16
- Ren T., Jiang B., Ren Y., Yang M., 2022, *Universe*, **8**, 465

- Rezaeikh S., Javadi A., Khosroshahi H., van Loon J. T., 2014, *MNRAS*, **445**, 2214
- Rocha-Pinto H. J., Majewski S. R., Skrutskie M. F., Crane J. D., Patterson R. J., 2004, *ApJ*, **615**, 732
- Rocha M., Peter A. H. G., Bullock J., 2012, *MNRAS*, **425**, 231
- Rosenfield P., et al., 2014, *ApJ*, **790**, 22
- Sakai S., Madore B. F., Freedman W. L., 1996, *ApJ*, **461**, 713
- Saremi E., et al., 2020, *ApJ*, **894**, 135
- Saremi E., Javadi A., Navabi M., van Loon J. T., Khosroshahi H. G., Bojnordi Arbab B., McDonald I., 2021, *ApJ*, **923**, 164
- Schlafly E. F., Finkbeiner D. P., 2011, *ApJ*, **737**, 103
- Schlegel D. J., Finkbeiner D. P., Davis M., 1998, *ApJ*, **500**, 525
- Shi J., et al., 2020, *ApJ*, **893**, 139
- Simha V., Weinberg D. H., Conroy C., Davé R., Fardal M. A., Katz N., Oppenheimer B. D., 2014, arXiv: Astrophysics of Galaxies
- Simpson C. M., Grand R. J. J., Gómez F. A., Marinacci F., Pakmor R., Springel V., Campbell D. J. R., Frenk C. S., 2018, *MNRAS*, **478**, 548
- Stetson P. B., 1987, *PASP*, **99**, 191
- Stetson P. B., 1990, *PASP*, **102**, 932
- Stetson P. B., 1994, Publications of the Astronomical Society of the Pacific, **106**, 250
- Stetson P. B., 1996, *PASP*, **108**, 851
- Tollerud E. J., et al., 2012, *ApJ*, **752**, 45
- Tolstoy E., 2003, *Ap&SS*, **284**, 579
- Valiante R., Schneider R., Bianchi S., Andersen A. C., 2009, *MNRAS*, **397**, 1661
- Vassiliadis E., Wood P. R., 1993, *ApJ*, **413**, 641
- Weisz D. R., Dolphin A. E., Skillman E. D., Holtzman J., Gilbert K. M., Dalcanton J. J., Williams B. F., 2014, *ApJ*, **789**, 147
- Weisz D. R., et al., 2019a, *MNRAS*, **489**, 763
- Weisz D. R., et al., 2019b, *ApJL*, **885**, L8
- Welch D. L., Stetson P. B., 1993, *AJ*, **105**, 1813
- Wetzel A. R., Tollerud E. J., Weisz D. R., 2015, *ApJL*, **808**, L27
- Wheeler C., et al., 2019, *MNRAS*, **490**, 4447
- Whitelock P., Feast M., Catchpole R., 1991, *MNRAS*, **248**, 276
- Whitelock P. A., Feast M. W., van Loon J. T., Zijlstra A. A., 2003, *MNRAS*, **342**, 86
- Whitelock P. A., Kasliwal M., Boyer M., 2017, *EPJ Web of Conferences*, **152**, 01009
- Wojno J., Gilbert K. M., Kirby E. N., Escala I., Beaton R. L., Tollerud E. J., Majewski S. R., Guhathakurta P., 2020, *ApJ*, **895**, 78
- Wood P. R., 1998, *A&A*, **338**, 592
- Wood P. R., Whiteoak J. B., Hughes S. M. G., Bessell M. S., Gardner F. F., Hyland A. R., 1992, *ApJ*, **397**, 552
- Xu H., Wise J. H., Norman M. L., Ahn K., O'Shea B. W., 2016, *ApJ*, **833**, 84
- Zijlstra A. A., Loup C., Waters L. B. F. M., Whitelock P. A., van Loon J. T., Guglielmo F., 1996, *MNRAS*, **279**, 32
- Zucker D. B., et al., 2004, *ApJL*, **612**, L121
- van Loon J. T., Groenewegen M. A. T., de Koter A., Trams N. R., Waters L. B. F. M., Zijlstra A. A., Whitelock P. A., Loup C., 1999, *A&A*, **351**, 559
- van Loon J. T., Cioni M. R. L., Zijlstra A. A., Loup C., 2005a, *A&A*, **438**, 273
- van Loon J. T., Marshall J. R., Zijlstra A. A., 2005b, *A&A*, **442**, 597
- van Loon J. T., Cohen M., Oliveira J. M., Matsuura M., McDonald I., Sloan G. C., Wood P. R., Zijlstra A. A., 2008, *A&A*, **487**, 1055

Table 6. Characterizing of variable candidates.

id	R.A. (J2000)	Dec (J2000)	V (mag)	δV (mag)	i (mag)	δi (mag)	amplitude $_i$ (mag)	M_{Birth} (M_{\odot})	τ_i	\dot{M} ($10^{-6} M_{\odot} \text{ yr}^{-1}$)	L ($10^4 L_{\odot}$)	chemical type
4957	00 52 40.39	+43 06 37.20	23.26	0.08	22.68	0.06	0.56	0.95	0.30	2.11	0.19	O
2686	00 53 25.47	+43 15 19.35	21.35	0.03	20.77	0.01	0.32	1.73	0.13	7.61	0.88	C
4837	00 52 49.79	+43 10 51.66	21.89	0.02	21.29	0.04	0.30	0.93	0.25	1.42	0.19	O
4799	00 52 49.13	+43 13 21.94	21.93	0.03	21.32	0.02	0.30	0.97	0.20	5.09	0.38	O
4601	00 53 18.14	+43 15 05.66	22.34	0.03	21.70	0.01	0.64	0.80	0.36	0.17	0.13	O
3543	00 53 13.45	+43 13 31.77	22.91	0.08	22.27	0.07	0.67	0.89	0.48	0.37	0.10	O
3481	00 52 13.34	+43 13 02.46	21.40	0.03	20.70	0.01	0.29	2.10	0.38	9.06	0.79	C
4973	00 52 52.45	+43 11 18.77	22.22	0.06	21.44	0.01	0.32	0.87	0.60	0.37	0.14	O
4901	00 53 11.49	+43 16 21.95	22.56	0.07	21.77	0.03	0.54	0.83	0.50	0.31	0.15	O
4448	00 52 55.29	+43 10 27.09	21.99	0.03	21.20	0.00	0.51	2.10	0.22	8.71	0.62	C
4190	00 52 33.54	+43 12 17.17	21.60	0.01	20.77	0.00	0.72	2.90	0.34	18.74	0.89	C
3798	00 52 48.01	+43 07 33.08	21.35	0.01	20.50	0.02	0.65	1.53	0.15	1.53	0.43	C
6338	00 52 46.09	+43 09 05.12	21.90	0.02	21.02	0.03	1.11	0.93	0.40	0.81	0.24	O
3236	00 52 36.14	+43 10 11.38	21.74	0.09	20.85	0.04	0.29	1.72	0.20	5.73	0.47	C
4757	00 53 00.79	+43 10 03.84	22.11	0.02	21.16	0.04	1.30	0.97	0.65	4.69	0.32	O
3919	00 53 23.70	+43 14 25.45	21.56	0.07	20.61	0.01	0.43	1.91	0.28	8.57	0.89	C
4951	00 52 39.94	+43 09 55.47	22.15	0.05	21.20	0.05	0.41	0.93	0.51	0.95	0.19	O
5284	00 52 59.36	+43 12 04.35	22.32	0.06	21.36	0.05	0.56	0.93	0.65	0.70	0.19	O
5073	00 53 29.77	+43 09 25.70	22.67	0.04	21.69	0.03	1.01	0.81	0.66	0.28	0.13	O
4770	00 52 53.68	+43 13 41.74	22.33	0.07	21.33	0.04	1.07	0.81	0.60	0.23	0.10	O
4435	00 52 54.35	+43 13 43.06	22.33	0.06	21.33	0.03	1.20	0.95	0.65	2.30	0.29	O
4127	00 52 34.93	+43 11 22.88	21.81	0.01	20.80	0.01	0.82	2.10	0.52	5.01	0.48	C
4250	00 53 00.93	+43 11 21.29	22.15	0.07	21.14	0.05	0.91	1.53	0.14	2.68	0.54	C
4512	00 52 59.41	+43 10 35.64	22.27	0.04	21.16	0.04	1.22	0.91	0.66	0.60	0.21	O
5339	00 53 01.96	+43 09 00.93	21.56	0.06	20.42	0.01	0.62	2.20	0.29	14.56	0.99	C
4349	00 52 06.19	+43 13 30.85	21.80	0.06	20.64	0.01	0.46	0.97	0.65	3.11	0.30	O
4573	00 52 20.74	+43 09 21.40	21.91	0.06	20.75	0.02	0.32	1.93	0.37	5.72	0.77	C
3703	00 52 36.50	+43 09 43.58	22.03	0.07	20.86	0.01	1.02	2.00	0.34	6.69	0.56	C
3824	00 52 51.91	+43 12 15.05	22.72	0.04	21.44	0.06	1.12	0.83	0.45	0.26	0.15	O
3010	00 53 03.48	+43 09 08.18	21.76	0.03	20.40	0.02	0.68	1.70	0.35	4.85	0.72	C
5503	00 52 14.24	+43 08 31.38	21.85	0.01	20.50	0.01	0.40	1.90	0.55	5.01	1.12	C
3416	00 52 10.98	+43 13 22.30	22.15	0.05	20.71	0.05	0.22	1.50	0.41	2.65	0.35	C
3587	00 52 23.64	+43 08 45.66	22.16	0.01	20.71	0.04	1.14	2.20	0.74	16.41	0.52	C

id	R.A. (J2000)	Dec (J2000)	V (mag)	δV (mag)	i (mag)	δi (mag)	amplitude _{i} (mag)	M_{Birth} (M_{\odot})	τ_i	\dot{M} ($10^{-6} M_{\odot} \text{ yr}^{-1}$)	L ($10^4 L_{\odot}$)	chemical type
5437	00 52 54.34	+43 12 40.17	23.00	0.08	21.46	0.07	0.90	0.91	0.98	0.61	0.14	O
5325	00 52 47.61	+43 11 08.23	22.91	0.06	21.31	0.05	1.90	0.90	0.67	0.45	0.16	O
4388	00 52 45.19	+43 11 49.30	22.97	0.07	21.32	0.06	1.43	1.55	0.50	3.02	0.63	C
4381	00 53 01.70	+43 06 45.22	22.16	0.05	20.42	0.01	0.75	1.70	0.50	3.49	0.35	C
4550	00 52 56.15	+43 12 22.27	23.31	0.09	21.57	0.07	1.32	0.85	0.99	0.27	0.13	O
5546	00 53 00.38	+43 14 10.44	23.38	0.10	21.62	0.06	0.96	0.83	0.95	0.26	0.12	O
4925	00 52 55.79	+43 12 38.16	23.30	0.07	21.49	0.06	1.72	2.80	0.70	18.26	0.69	C
4541	00 52 52.66	+43 15 12.78	23.61	0.07	21.80	0.02	1.41	0.89	0.97	0.42	0.19	O
5848	00 53 25.79	+43 10 20.78	22.18	0.01	20.35	0.00	1.31	2.60	0.60	17.04	1.04	C
5030	00 52 43.08	+43 14 32.50	23.83	0.05	21.86	0.04	1.00	2.00	1.02	0.21	0.08	C
4151	00 52 48.26	+43 08 49.87	22.98	0.01	21.00	0.01	1.23	0.83	0.67	6.90	0.40	O
3243	00 52 22.35	+43 06 58.08	23.11	0.07	20.95	0.00	1.16	0.90	0.87	2.67	0.30	O
5493	00 53 00.08	+43 07 44.17	22.63	0.06	20.42	0.02	2.20	2.20	0.70	15.67	1.07	C
4357	00 53 09.67	+43 10 44.04	22.61	0.05	20.36	0.00	1.41	2.60	0.70	18.18	1.20	C
4839	00 53 02.26	+43 14 47.48	23.89	0.06	21.59	0.01	1.62	0.83	1.20	0.21	0.09	O
5671	00 52 54.62	+43 10 01.29	23.30	0.08	20.91	0.06	1.55	1.55	0.85	2.39	0.26	C
4433	00 53 08.08	+43 15 01.26	22.91	0.06	20.36	0.04	1.76	1.82	0.87	6.16	0.46	C



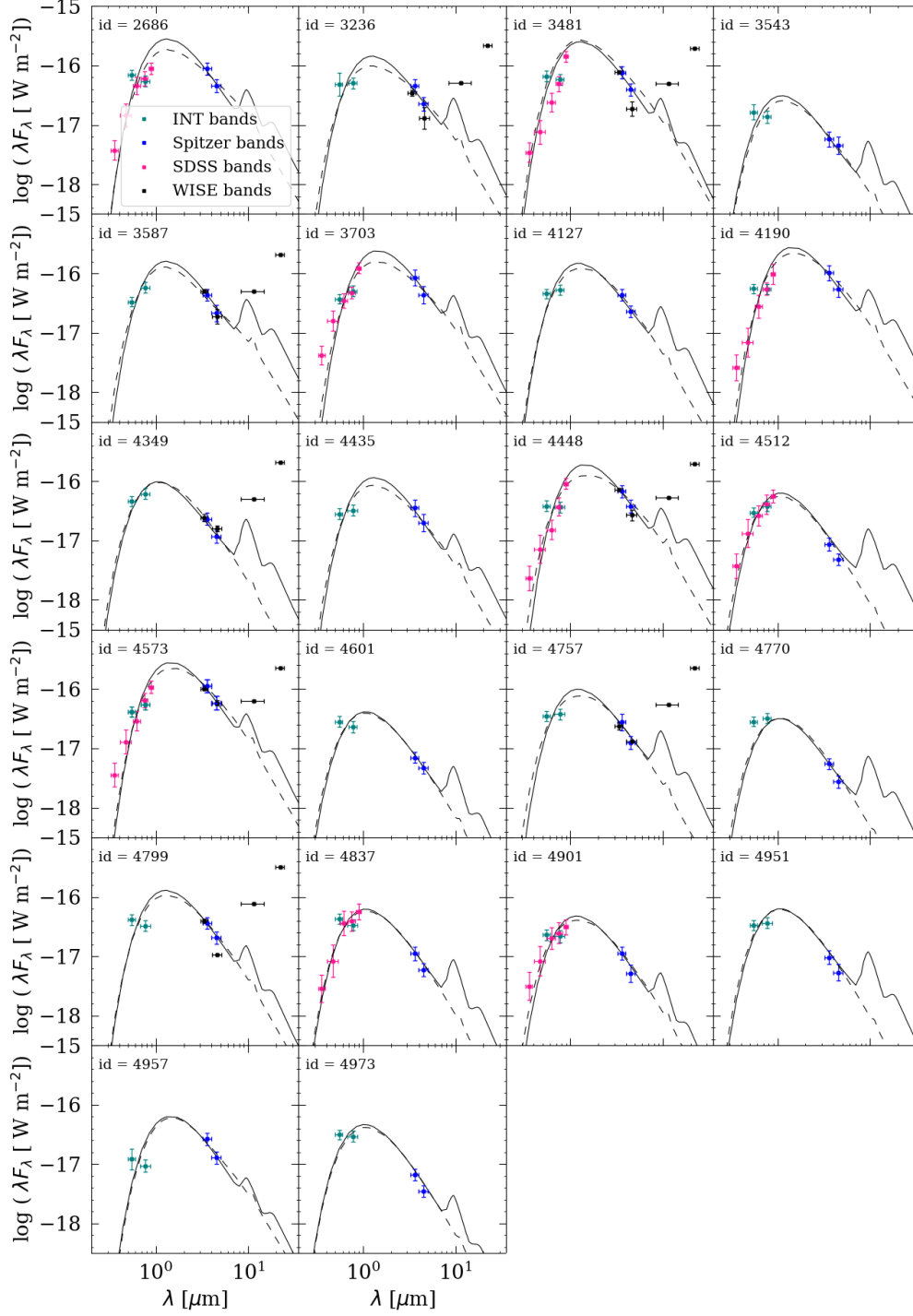


Figure 28. SEDs of LPVs with the best fit for the C- and O-rich type of AGBs (dashed and solid black lines). Fluxes are modelled by `DUSTY` as a function of wavelength. Fluxes observed in different bands with the INT (*i* and *V*), *Spitzer* (3.6 and 4.5 μm), SDSS (*u*, *g*, *r*, *i*, and *z*), and WISE (*W*₁, *W*₂, *W*₃, and *W*₄) are shown by green, blue, pink, and black squares, respectively. Vertical and horizontal error bars show photometric uncertainty in the magnitude and the difference between the λ_{max} and λ_{min} around each filter's central wavelength, respectively.